

Physics of the Isotopic Dependence of Galactic Cosmic Ray Fluence Behind Shielding

*Francis A. Cucinotta, Premkumar B. Saganti, Xiaodong Hu,
Myung-Hee Y. Kim, and Timothy F. Cleghorn
NASA Johnson Space Center
Houston TX, 77058*

*John W. Wilson and Ram K. Tripathi
NASA Langley Research Center
Hampton VA, 23664*

*Cary J. Zeitlin
Lawrence Berkeley National Laboratory
Berkeley, CA 94720*

The NASA STI Program Office . . . in Profile

Since its founding, NASA has been dedicated to the advancement of aeronautics and space science. The NASA Scientific and Technical Information (STI) Program Office plays a key part in helping NASA maintain this important role.

The NASA STI Program Office is operated by Langley Research Center, the lead center for NASA's scientific and technical information. The NASA STI Program Office provides access to the NASA STI Database, the largest collection of aeronautical and space science STI in the world. The Program Office is also NASA's institutional mechanism for disseminating the results of its research and development activities. These results are published by NASA in the NASA STI Report Series, which includes the following report types:

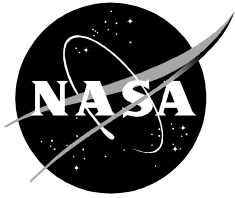
- **TECHNICAL PUBLICATION.** Reports of completed research or a major significant phase of research that present the results of NASA programs and include extensive data or theoretical analysis. Includes compilations of significant scientific and technical data and information deemed to be of continuing reference value. NASA's counterpart of peer-reviewed formal professional papers but has less stringent limitations on manuscript length and extent of graphic presentations.
- **TECHNICAL MEMORANDUM.** Scientific and technical findings that are preliminary or of specialized interest, e.g., quick release reports, working papers, and bibliographies that contain minimal annotation. Does not contain extensive analysis.
- **CONTRACTOR REPORT.** Scientific and technical findings by NASA-sponsored contractors and grantees.

- **CONFERENCE PUBLICATION.** Collected papers from scientific and technical conferences, symposia, seminars, or other meetings sponsored or cosponsored by NASA.
- **SPECIAL PUBLICATION.** Scientific, technical, or historical information from NASA programs, projects, and mission, often concerned with subjects having substantial public interest.
- **TECHNICAL TRANSLATION.** English-language translations of foreign scientific and technical material pertinent to NASA's mission.

Specialized services that complement the STI Program Office's diverse offerings include creating custom thesauri, building customized databases, organizing and publishing research results . . . even providing videos.

For more information about the NASA STI Program Office, see the following:

- Access the NASA STI Program Home Page at <http://www.sti.nasa.gov>
- E-mail your question via the Internet to help@sti.nasa.gov
- Fax your question to the NASA Access Help Desk at (301) 621-0134
- Telephone the NASA Access Help Desk at (301) 621-0390
- Write to:
NASA Access Help Desk
NASA Center for AeroSpace Information
7121 Standard
Hanover, MD 21076-1320



Physics of the Isotopic Dependence of Galactic Cosmic Ray Fluence Behind Shielding

*Francis A. Cucinotta, Premkumar B. Saganti, Xiaodong Hu,
Myung-Hee Y. Kim, and Timothy F. Cleghorn
NASA Johnson Space Center
Houston TX, 77058*

*John W. Wilson and Ram K. Tripathi
NASA Langley Research Center
Hampton VA, 23664*

*Cary J. Zeitlin
Lawrence Berkeley National Laboratory
Berkeley, CA 94720*

National Aeronautics and
Space Administration

Johnson Space Center
Houston, Texas 77058-3696

Available from:

NASA Center for AeroSpace Information
7121 Standard
Hanover, MD 21076-1320

National Technical Information Service
5285 Port Royal Road
Springfield, VA 22161

This report is also available in electronic form at <http://techreports.larc.nasa.gov/cgi-bin/NTRS>

CONTENTS

Abstract	1
Introduction	1
Isotopic Composition of the GCR	4
Isotopic Effects in GCR Transport.....	8
Isotopic Effects in Quantum Fragmentation Model.....	9
Results	15
Discussion.....	26
Acknowledgments	27
References.....	28

Tables

1a	Comparison of HZETRN to Flight Measurements on NASA Space Shuttle and Russian Mir Space Station	32
1b	Comparisons of HZETRN Code to NASA Space Shuttle Phantom Torso Experiment on STS-91	32
2a	Isotopic Composition of GCR Elements $Z=3$ to 12	33
2b	Isotopic Composition of GCR Elements $Z=13$ to 20	34
2c	Isotopic Composition of GCR Elements $Z=22$ to 26	35
3a	Isotopic Grid used in Present HZETRN Calculations for Elements $Z=0-8$	36
3b	Isotopic Grid used in Present HZETRN Calculations for Elements $Z=9-14$..	37
3c	Isotopic Grid used in Present HZETRN Calculations for Elements $Z=15-19$	38
3d	Isotopic Grid used in Present HZETRN Calculations for Elements $Z=20-23$	39
3e	Isotopic Grid used in Present HZETRN Calculations for Elements $Z=24-28$	40
4a	Elemental (Z) and Neutron Excess (Y) Dependence on GCR Dose Equivalent Behind 0 g/cm^2 of Aluminum Shielding	41
4b	Elemental (Z) and Neutron Excess (Y) Dependence on GCR Dose Equivalent Behind 5 g/cm^2 of Aluminum Shielding	42
4c	Elemental (Z) and Neutron Excess (Y) Dependence on GCR Dose Equivalent Behind 20 g/cm^2 of Aluminum Shielding	43
5	Annual Fluence of Several Unstable GCR Nuclei Versus Depth of Aluminum Shielding Near Solar Minimum ($\Phi=428 \text{ MV}$)	44

Figures

1	Comparison of HZETRN code predictions to MARIE experiment on Odyssey orbiting Mars.....	2
2	Parametric model for describing the change in isotopic composition with the solar modulation parameter, Φ (V).....	6
3a	Energy spectra for hydrogen and helium isotopes near solar minimum ($F=428$ MV) and solar maximum ($\Phi=1050$ MV)	7
3b	Energy spectra for Ne, Si, and Fe isotopes near solar minimum ($\Phi=428$), showing contributions from different isotopes to primary GCR composition.	7
4	Abrasion cross-sections versus impact parameter for $n=1, 2, 4$, and 12 nucleon removal in ^{32}S fragmentation at 0.1 GeV/u on Al targets showing the corrections for Coulomb trajectories and the in-medium nucleon-nucleon interaction	14
5	Comparisons of the QMSFRG model to experiment for elemental fragment distribution for ^{20}Ne on ^{12}C at 0.6 GeV/u	15
6	Comparisons of the QMSFRG model to experiment for the elemental fragment distribution for ^{22}Ne on ^1H at 0.894 GeV/u.....	16
7	Comparisons of the QMSFRG model to experiment for the elemental fragment distribution for ^{26}Mg on ^1H at 0.576 GeV/u	17
8	Comparisons of the QMSFRG model to experiment for the elemental fragment distribution for ^{27}Al on ^{12}C at 0.582 GeV/u.....	17
9	Comparisons of the QMSFRG model to experiment for the elemental fragment distribution for ^{28}Si on ^{12}C at 0.6 GeV/u.....	18
10	Comparisons of the QMSFRG model to experiment for the elemental fragment distribution for ^{32}S on ^{27}Al at 1.2 GeV/u	18
11	Comparisons of the QMSFRG model to experiment for the elemental fragment distribution for ^{36}Ar on ^1H at 0.765 GeV/u.....	19
12	Comparisons of the QMSFRG model to experiment for the elemental fragment distribution for ^{40}Ar on ^1H at 0.352 GeV/u.....	19
13	Comparisons of the QMSFRG model to experiment for the elemental fragment distribution for ^{40}Ca on ^{12}C at 0.763 GeV/u	20
14	Comparisons of the QMSFRG model to experiment for the elemental fragment distribution for ^{52}Cr on ^1H at 0.338 GeV/u.....	20
15	Comparisons of the QMSFRG model to experiment for the elemental fragment distribution for ^{56}Fe on ^{12}C at 1.05 GeV/u.....	21
16	Comparisons of the QMSFRG model to experiment for the elemental fragment distribution for ^{56}Fe on ^{27}Al at 1.05 GeV/u	21
17	Comparisons of the QMSFRG model to experiment for distribution of fragments for ^{40}Ar on ^{12}C at 0.6 GeV/u.....	22

18	Comparisons of the QMSFRG model to experiment for the elemental distribution of fragments from ^{56}Fe on ^{12}C at 0.6 GeV/u	22
19	Comparisons of results from the HZETRN code for the mass flux distribution behind 5 g/cm ² of aluminum shielding for solar minimum conditions comparing transport with the reduced 59-isotope grid to transport with a full 170-isotope grid	23
20	Comparisons of the error that results from the HZETRN code for the mass fluence distribution near solar minimum when using a reduced 59-isotope grid compared to transport with a 170-isotope grid	24
21	Comparisons of the error that results from the HZETRN code for the elemental fluence distribution near solar minimum when using a reduced 59-isotope grid compared to transport with a 170-isotope grid	25
22	Comparisons of the error that results from the HZETRN code for the mass fluence distribution near solar maximum when using a reduced 59-isotope grid compared to transport with a 170-isotope grid	25
23	Comparisons of the error that results from the HZETRN code for the elemental fluence distribution near solar maximum when using a reduced 59-isotope grid compared to transport with a 170-isotope grid	26

ABSTRACT

For over 25 years, NASA has supported the development of space radiation transport models for shielding applications. The NASA space radiation transport model now predicts dose and dose equivalent in Earth and Mars orbit to an accuracy of $\pm 20\%$. However, because larger errors may occur in particle fluence predictions, there is interest in further assessments and improvements in NASA's space radiation transport model. In this paper, we consider the effects of the isotopic composition of the primary galactic cosmic rays (GCR) and the isotopic dependence of nuclear fragmentation cross-sections on the solution to transport models used for shielding studies. Satellite measurements are used to describe the isotopic composition of the GCR. Using NASA's quantum multiple-scattering theory of nuclear fragmentation (QMSFRG) and high-charge and energy (HZETRN) transport code, we study the effect of the isotopic dependence of the primary GCR composition and secondary nuclei on shielding calculations. The QMSFRG is shown to accurately describe the iso-spin dependence of nuclear fragmentation. The principal finding of this study is that large errors ($\pm 100\%$) will occur in the mass-fluence spectra when comparing transport models that use a complete isotope grid (~ 170 ions) to ones that use a reduced isotope grid, for example the 59 ion-grid used in the HZETRN code in the past, however less significant errors ($< 20\%$) occur in the elemental-fluence spectra. Because a complete isotope grid is readily handled on small computer workstations and is needed for several applications studying GCR propagation and scattering, it is recommended that they be used for future GCR studies.

INTRODUCTION

An important goal for NASA's Space Radiation Health Program is to develop a predictive capability to predict the galactic cosmic rays (GCR) fluence spectra to within a $\pm 25\%$ accuracy (Anon., 1998). NASA has developed the HZETRN (high-charge and energy transport) code (Wilson, 1977; Wilson and Badavi, 1986; Wilson *et al.*, 1991, 1995a) as a science application and engineering design tool (Wilson *et al.*, 1993) to be used in space radiation shielding studies. HZETRN has been validated in its ability to predict total dose and dose equivalent behind several materials in space to within $\pm 20\%$ on multiple space missions in Earth orbit (**Table 1**) and the MARIE experiment on the Odyssey spacecraft in Mars orbit (**Figure 1**) (Cucinotta *et al.*, 2000a, Badhwar and Cucinotta, 2000, Badhwar *et al.*, 2001, Zeitlin, *et al.*, 2002, <http://srhp.jsc.nasa.gov>). However, interest in

fluence-based approaches to risk assessment (Cucinotta *et al.*, 1995a, 1996a) suggests that more stringent tests of transport code accuracy need to be made, and the quantities dose and dose equivalent are deemed as necessary, but not sufficient tests of their accuracy. In this regard, we note that dose and dose equivalent are integral quantities that receive contributions from many GCR charge groups. Large uncertainties currently exist in radiation quality factors (Cucinotta, *et al.*, 2001) and current methodologies to estimate health risks such that dose and dose equivalent may be insufficient as tests of transport code accuracy. The use of ion fluence as a basis for tests for accuracy provides for sufficient generality to ensure accuracy in GCR transport models, including under the circumstances of revision of radiation quality factors or integration of alternative risk assessment approaches in the future.

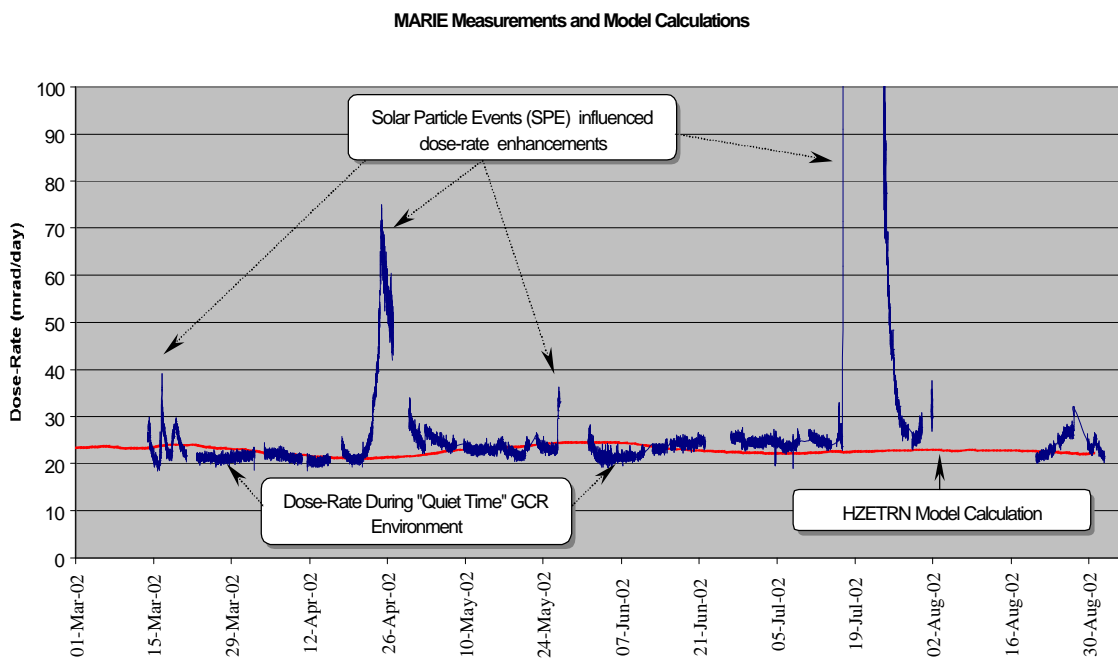


Figure 1: Comparison of HZETRN code predictions to MARIE experiment (Zeitlin *et al.*, 2003) on Odyssey orbiting Mars.

In the description of the transport of the GCR in shielding materials or tissue, a common approximation used in the past is to consider only the elemental composition of the primary GCR and a reduced isotope grid for the secondary nuclei produced in nuclear fragmentation. In this paper, we analyze the role of the isotopic dependence of the GCR primary composition and nuclear fragmentation in predicting the fluence of the GCR behind arbitrary shielding configurations. Our study is an important milestone in achieving NASA's goal of accurate GCR transport codes since, for the first time, a complete isotope grid has been achieved in a GCR transport model and we document the error inherent in former approaches. Also, for applications that will consider radioactive isotopes produced in the atmosphere or shielding, our study provides a

useful tool to perform such analyses. Other applications where non-stable nuclei are considered are studies of the origin of the GCR where so-called cosmic-ray “clocks” consider the primary or secondary GCR with life-times on the order of confinement time in the galaxy (~ 1 M-yrs) (Yanasak *et al.*, 1999). Several GCR “clock” nuclei, including ^{10}Be and ^{26}Al , were not considered in the isotope grid used in HZETRN in the past. Finally, the MARIE experiment orbiting Mars on the Odyssey spacecraft (Badhwar, 2003, and Zeitlin *et al.*, 2003) is collecting new data on the GCR environment near Mars, and our study provides an opportunity to begin new investigations on the accuracy of computational models used to describe the GCR environment.

Historically, the HZETRN code grew from a 29-ion isotope grid used in the 1980s and early 1990s (Wilson, *et al.*, 1991) to an extension to a 32-ion isotope grid made in 1993 in order to include all light ions (Cucinotta, 1993). Because of the limitations of random access memory (RAM) present on the computer workstations of the early 1990s, sensitivity studies were made for mono-energetic ion beams to study the minimum number of isotopes for convergence, resulting in the use of 59-isotope grid (Kim, *et al.*, 1994), and all GCR studies since 1994 have used the 59-isotope grid (Shinn, *et al.*, 1994). However, there are several reasons to reconsider the use of the full isotope grid for GCR transport problems. First, the isotopic dependence of the primary GCR has not been considered in past shielding studies and may lead to errors in the description of both primary ion attenuation and secondary particle production, including the role of high-energy neutron production from the many neutron-rich species that occur. Secondly, the studies of Kim *et al.* (1994) used the NUCFRG2 model of fragmentation (Wilson *et al.*, 1994), which does not provide a correct description of the even-odd effect observed in fragment production or of the projectile iso-spin dependence observed experimentally (Knott *et al.*, 1996, 1997; Zeitlin *et al.*, 2001). Thirdly, the sensitivity studies made by Kim *et al.* (1994) used a “calibration” of the isotope grid to ^{56}Fe beams; however a larger isotope grid occurs when all GCR projectile nuclei are considered. Fourth, the error in the range-energy and stopping powers that results from the use of a reduced isotope grid, although expected to be small for large mass numbers, $A \gg 1$, is an unnecessary one for transport calculations. Finally, the improved computational speed and memory available on current small computer workstations makes including a complete isotope grid in the HZETRN code possible.

In this paper, we describe the implementation of the HZETRN code to include the full isotopic dependence of the primary GCR. We describe the physics of isotopic effects in GCR transport, and the fragmentation parameters are a key component of this description. The quantum multiple scattering theory of nuclear fragmentation (QMSFRG) is used as the generator for fragmentation cross-sections used in our study. An empirical model of the isotopic composition of the primary GCR, including its solar modulation, is also described. For GCR problems, we identified an isotope grid of 170 ions and made comparisons to previous HZETRN results using the reduced-grid of 59 isotopes. We note that a preliminary version of this report used an isotope grid of 141 ions (Cucinotta, 2002), which has been expanded in this current work. The

present code includes all of the abundant nuclei in the GCR environment with fluxes greater than about $10^2/\text{cm}^2/\text{yr}$ and nuclei produced in fragmentation events with production cross-sections greater than about 1 mb. Several nuclei with smaller primary abundances or production cross-sections, which are of interest for scientific reasons are also included in the expanded HZETRN model described herein. The resultant code includes many neutron-rich nuclei that have been ignored in the past with iso-spin components ranging from $T_z = +3/2$ to $T_z = -3$.

ISOTOPIC COMPOSITION OF THE GCR

NASA currently uses the GCR model of Badhwar and O'Neill (1992) to describe the elemental composition and energy spectra of the GCR, including their modulation by the Sun's magnetic field. In this GCR representation, we considered only the most abundant GCR nuclei for each element and counted other isotopes of identical charge as the abundant isotope. However, theoretical models and satellite measurements of the GCR have long considered the isotopic composition of the GCR and their modification through transport in interstellar space, including estimating the primary nuclear composition at stellar sources (Parker, 1965, Webber *et al.*, 1990a, Fields *et al.*, 1994). The approach used here is to estimate an energy-independent isotopic fraction, f_j from satellite measurements, which are constrained to obey the sum rule

$$(1) \quad f(Z, E) = \sum_{A_j} f_j f(A_j, Z, E)$$

where the left-hand side of eq. (1) is the elemental spectra from the Badhwar and O'Neill model and $\sum_j f_j = 1$. Equation (1) is used herein as an initial estimate of the influence of the primary isotopic composition on GCR shielding calculations. Experimental studies have included measurements on the Pioneer, Voyager, and Ulysses spacecraft. A survey of such data (Hesse *et al.*, 1991; Lukasiak, *et al.*, 1993, 1995; Webber *et al.*, 1985, 1990; Wiedenback *et al.*, 1981, 1985) was made, with the results shown in **Table 2**. For this compilation, we note that, since secondary fragment production is modulated by the transit time in the heliosphere, the isotopic fraction is dependent on the position in the solar cycle. In **Table 2** we have used data on isotopic fractions near solar maximum where the isotopic fraction for nuclei produced within the heliosphere are expected to be at a maximum (Hesse *et al.*, 1991; Lukasiak *et al.*, 1993; Webber *et al.*, 1985, 1990; Wiedenback *et al.*, 1981, 1985). For several elements listed in **Table 2**, information on solar modulation was not available and isotopic fractions for near-Earth and GCR sources were set identical, using the near-Earth estimate.

We next discuss some areas of interest for understanding the GCR isotopic composition. The GCR path-length distribution represents the mean amount of interstellar and interplanetary material intersected by cosmic rays prior to their arrival in the near-Earth environment. This distribution is currently estimated to vary between 3 and 20 g/cm² of approximately 90% H and

10% He. The variability in the estimates is because they are model-dependent on nuclear fragmentation parameters, cosmological interaction terms, and factors related to the near-Earth or deep space measurements, including energy and mass resolution of the detectors as well as position in the solar cycle. In most current models, the GCR path-length distribution is estimated to be velocity- and rigidity-dependent (i.e., energy-dependent). A common form for the GCR path-length distribution is (Webber *et al.*, 1990a)

$$I = 10.8b\left(\frac{R}{R_0}\right)^{-0.6} \quad \text{for } R > 4GV; \quad I = 10.8b \quad \text{for } R \leq 4GV$$

where β is the velocity relative to the speed of light and R the rigidity.

Of note is that, based on the solar modulation theory of Parker (1965), the inter-planetary portion of this distribution would be modulated over the solar cycle, suggesting the form

$$I(\Phi, r) = I_{interstellar} + I_{interplanetary}(\Phi, r)$$

where Φ is the solar modulation parameter and r (in A.U.) is the radial distance from the Sun. It then follows that the isotopic abundances are dependent on the modulation parameter and radial distance, and will be energy-dependent. The so-called Leaky Box Model is the approach most often used to estimate the path-length distribution. Here the interstellar propagation of the GCR, including source terms, ionization and nuclear scattering terms as well as other cosmological interaction terms, is described. However the separation described above between scattering inside and outside of the heliosphere is not made. Because the path length is energy-dependent, the Leaky Box Model divides interstellar materials into slabs and uses weighted average over distinct energy bins to reconstruct the GCR abundances near Earth (or the inverse problem to reconstruct the source abundances). Such an approach is not easily implemented by the HZETRN code, but could be treated by the non-perturbative Green's function approach to HZE transport of Wilson *et al.* (1994). Herein, these considerations are not addressed and the solar modulation of the GCR abundances are treated in an energy-independent manner using empirical estimates based on satellite data. To go beyond the present or possibly alternative parametric approaches will require implementing the Leaky Box Model to create the boundary condition for the HZETRN shielding calculations.

Based on the results of Lukasiak *et al.* (1993). The following empirical formula is used to describe the dependence of the isotopic ratio (near-Earth) on the solar cycle including a dependence on the modulation parameter $F(MV)$

$$(2) \quad f(A, Z) = f_{Source}(A, Z) + [\exp(g\sqrt{\Phi}) - 1]$$

where g is found by interpolating from the source and near solar maximum values. The second term in eq. (2) can be positive or negative as dependent on the conditions for a net gain or reduction in the cosmic nuclei during transit from the galactic sources (Fields *et al.*, 1994) to the inner heliosphere. For the $Z=1$ and $Z=2$ ions, we use the following empirical formula to estimate the primary (near-Earth) ^2H and ^3He spectra

$$(3a) \quad f_{3\text{He}}(E) = \{0.0764 + 0.097 \exp[-0.5(\ln(E/1660)/1.306)^2]\} f_{4\text{He}}(E)$$

$$(3b) \quad f_{2\text{H}}(E) = 0.2 f_{4\text{He}}(E)$$

where $f_{3\text{He}}(E)$ and $f_{2\text{H}}(E)$ are subtracted from the Badhwar and O'Neill model (1992) for $f_{4\text{He}}(E)$ and $f_{1\text{H}}(E)$, respectively. **Figure 2** shows the assumed dependence of the isotope abundance scaling as a function on the solar modulation parameter described by eq. (3) for ^{13}C and ^{15}N . Similar results are found for other isotopes listed in **Table 2**. Examples of the GCR energy spectra for hydrogen and helium are shown in **Figure 3a** and for the isotopes of Ne, Si, and Fe at solar minimum in **Figure 3b**.

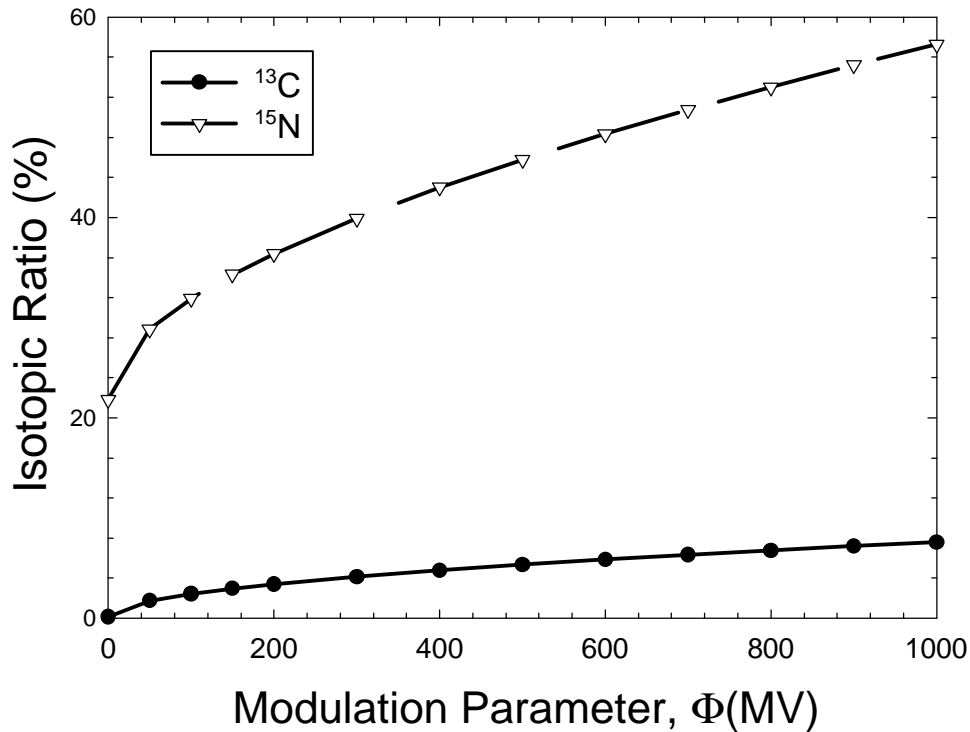


Figure 2: Parametric model for describing the change in isotopic composition with the solar modulation parameter, Φ (MV).

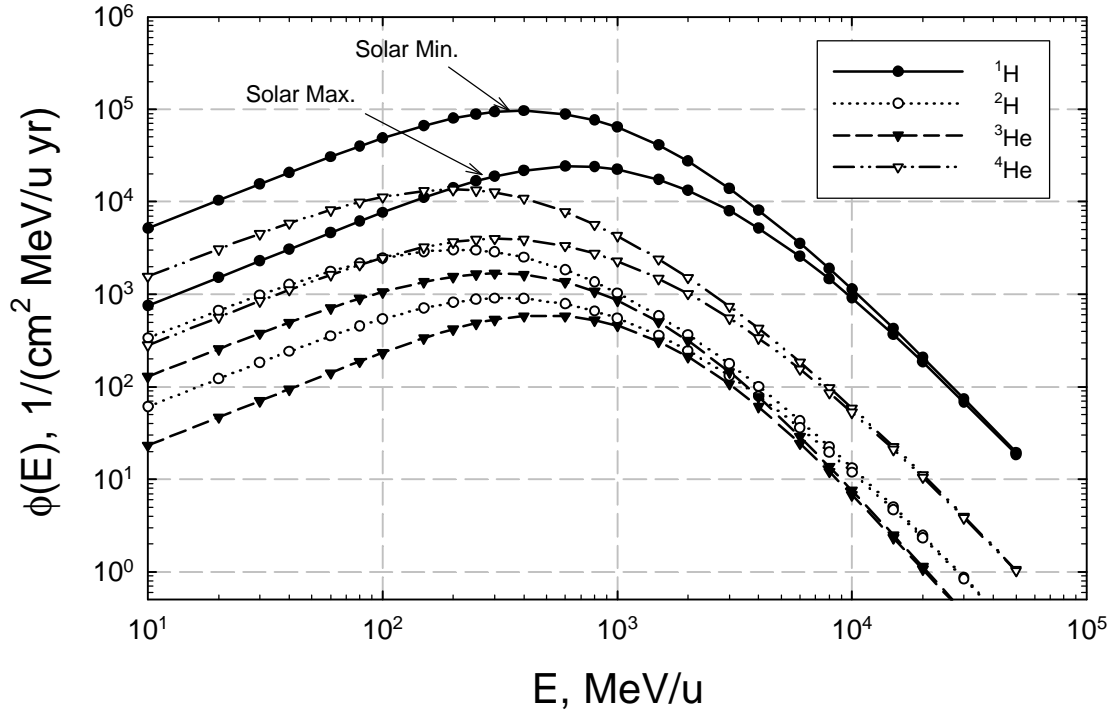


Figure 3a: Energy spectra for hydrogen and helium isotopes near solar minimum ($\Phi=428$ MV) and solar maximum ($\Phi=1050$ MV).

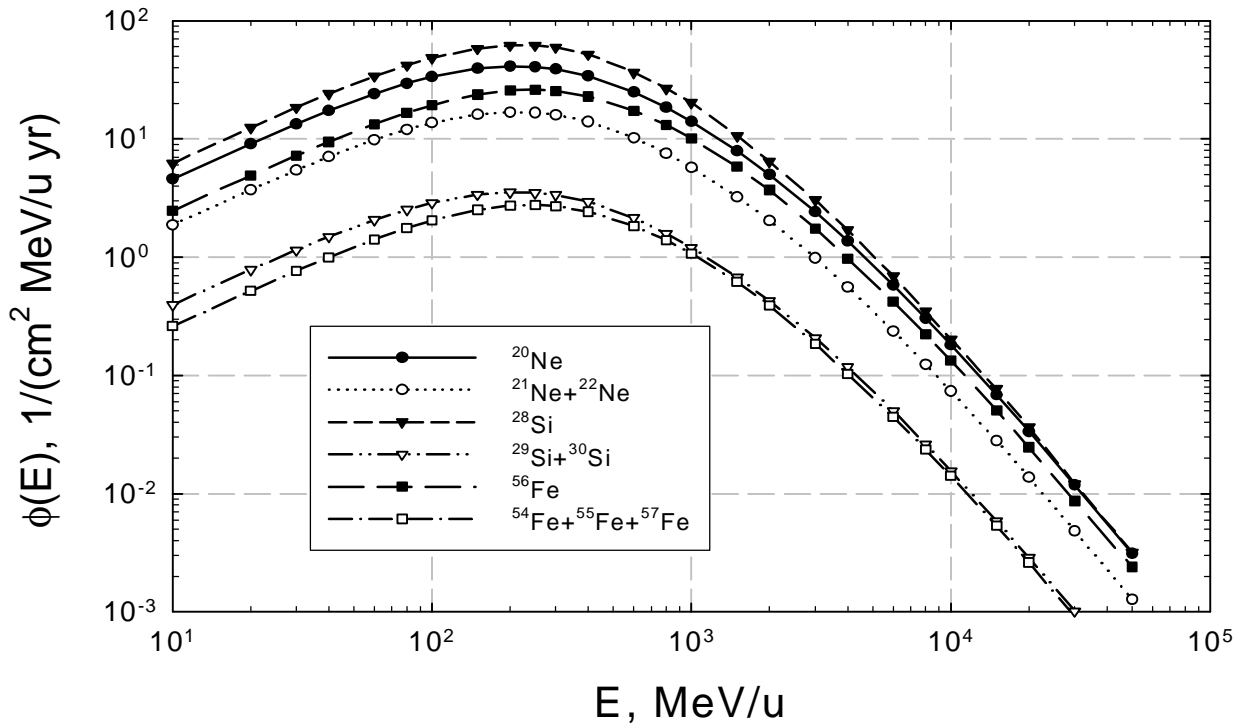


Figure 3b: Energy spectra for Ne, Si, and Fe isotopes near solar minimum ($\Phi=428$), showing contributions from different isotopes to primary GCR composition.

ISOTOPIC EFFECTS IN GCR TRANSPORT

The reduction of the full 3-dimensional (3D) Boltzmann transport equation within the straight-ahead and continuous slowing down approximations and assuming velocity conservative fragmentation events accurately describes the transport of GCR heavy ions (Wilson *et al.* 1986, 1991, 1995). In this model, the heavy ion flux, $f_j(E, x)$ of an ion j with mass number A_j , charge number Z_j , energy E (in units of MeV/u) at shielding depth x (in units of g/cm²) is determined by the partial differential equation (Wilson *et al.*, 1991)

$$(4) \quad \left[\frac{\partial}{\partial x} - \frac{1}{S_j(E)} \frac{\partial}{\partial E} + s_j(E) \right] f_j(x, E) = \sum_k s_{j,k}(E) f_k(E, x)$$

where $S_j(E)$ is the stopping power of ion j , $s_j(E)$ is the energy-dependent absorption cross-section (cm⁻¹) and $s_{jk}(E)$ is the fragmentation cross-section for producing an ion j from k . The solution to eq. (4) in the HZETRN code is found using the methods of characteristics where the coordinate transformation

$$(5) \quad h_j = x - R_j(E); \quad x_j = x + R_j(E)$$

and the scaled flux

$$(6) \quad c_j(h_j, x_j) = S_j(E) f_j(x, E)$$

are introduced, leading to the transport equation

$$(7) \quad \left[2 \frac{\partial}{\partial h_j} + s_j \right] c(h_j, x_j) = \sum_k s_{j,k} \frac{n_j}{n_k} c(h_k, x_k)$$

where $v_j = Z_j^2/A_j$. The numerical solution to equation (7) is implemented using a marching procedure as described by Wilson *et al.* (1990). The solution of the GCR transport equation for light ions and neutrons is distinct from eq. (7) because of the broad redistribution of energy in collision events and is described elsewhere (Wilson *et al.*, 1991, Cucinotta *et al.*, 1994a, and Cloudsley *et al.*, 2000).

Because eq. (7) is a coupled integro-differential equation for the many GCR primary and secondary nuclei, required computer memory allocations increase rapidly as the number of ion species is increased and was an important consideration in the early 1990s. However, such practical limitations no longer exist, even on small computer workstations with sufficient RAM

(e.g. Pentium III or higher), and an unrestricted isotope grid can presently be implemented with no memory or storage problems. When using a reduced isotope grid, fragments not contained in the grid are assigned to a nearby mass of identical charge number. This introduces two types of errors: First, the range-energy and stopping powers are altered from their true values. This error is expected to be small at high-energies for $A \gg 1$ since here ion ranges are well described by A/Z_j^2 scaling factors. The second type of error occurs in the absorption and fragmentation cross-sections. Here, because of the reassignment of the mass number when using a reduced grid, an error is introduced by the change in neutron number from its true values. Such errors arise from modifying the atomic transport properties and nuclear fragmentation cross-sections, and spectra of high-energy neutrons produced in fragmentation events from their true values by forcing the physics onto a reduced isotope grid. This latter error is expected to be small for heavy target nuclei ($A > 16$) because neutron production is dominated by light-particle (n , p , d , t , h , and α) interactions on target nuclei, but may be non-negligible for light target atoms ($A < 16$) (Cucinotta *et al.* 1998a). Since materials with high-hydrogen content are known to be the optimal shielding materials, the changes in the neutron fluence due to the use of a full isotope grid should be considered.

ISOTOPIC EFFECTS IN QUANTUM FRAGMENTATION MODEL

We next discuss the quantum multiple scattering description of heavy ion fragmentation (QMSFRG), which has been quite successful in describing the physics of the abrasion – ablation model of fragmentation and experimental data (Cucinotta, *et al.* 1994b, 1997, 1998b). The scattering amplitude for the heavy ion collision is related to the cross-section

by the phase space of each particle that appears in the final state. In the QMSFRG theory for inclusive reactions in which a single fragment originating in the projectile is measured, closure is performed on the final target state with a momentum vector denoted \mathbf{p}_X used to represent these states. The cross-section is then given by

$$(8) \quad d\sigma = \frac{(2\pi)^4}{\beta} \sum_X d\mathbf{p}_X d\mathbf{p}_{F^*} \sum_{n=1}^n \prod_{j=1}^n [d\mathbf{p}_j] \delta(E_i - E_f) \delta(\mathbf{p}_i - \mathbf{p}_f) |T_{fi}|^2$$

where \mathbf{b} is the relative projectile-target velocity, F^* represents the pre-fragments formed in the projectile-target interaction, n is the number of nucleons knocked out of the projectile in the overlap region with the target (Cucinotta, 1994c), and i and f label the initial and final states, respectively. The pre-fragments decay through particle emission if sufficient energy is available. To include the phase space of decay products of F^* , we write

$$(9) \quad d\mathbf{p}_{F^*} = d\mathbf{p}_F \prod_{r=0} d\mathbf{p}_r$$

where r is the ions (if any) emitted in the decay of the F^* . In considering nucleon production from the decay, we would study the \mathbf{p}_r (Cucinotta *et al.*, 1997b). The total momentum transfer is $\mathbf{q} = \mathbf{p}_T - \mathbf{p}_X$, where \mathbf{p}_T is the initial target momentum. We use the momentum conserving delta-function in eq. (8) to eliminate \mathbf{p}_F or one of the \mathbf{p}_{j_i} from eq. (8). The 3D inclusive cross-section for producing an ion F is given without approximation by

$$(10) \quad \frac{d\mathcal{S}}{d\mathbf{p}_F} = \frac{(2p)^4}{b} \sum_X \int d\mathbf{q} d\mathbf{p}_X \prod_{r=0} d\mathbf{p}_r \sum_{n=1} \prod_{j=1}^n [d\mathbf{p}_j] d(E_i - E_f) d(\mathbf{p}_i - \mathbf{p}_f) |T_{fi}|^2$$

For elastic scattering or the excitation of discrete states, the relation between the transition matrix T_{fi} and the inclusive cross-sections is trivial. For fragmentation reactions, where several to many particles are present in the final state, the integrals in eq. (10) become intractable and approximations must be introduced. One approach is to use a closure approximation on all unobserved projectile fragments, however at the expense of losing information on final state interactions among the projectile fragments. Real progress in reducing the multiparticle momentum integrals to a computationally feasible form is achieved only after studying the structure of the nucleus-nucleus transition matrix. The equations of motion for nuclear scattering are expressed in terms of the transition operator, which represents an infinite series for the multiple scattering of constituents of the projectile and target nucleon. The strong nature of the nuclear force requires a non-perturbative solution to the scattering problem. A relativistic theory is of interest for the space radiation databases, because of the high energies of the particles and the large number of production processes that are naturally included in a relativistic theory. A relativistically covariant formulation of the problem has been put forth by Maung and co-workers (1996) using meson exchange theory. The basic approach, in both relativistic and non-relativistic multiple scattering theories, is to re-sum the multiple scattering series, which is expressed in terms of the irreducible and reducible exchange diagrams in the RMST or the nuclear potential in the NRMST, in terms of the transition matrix for projectile and target nuclei constituents. This avoids having to deal directly with the highly singular behavior of the nuclear potential at short distances, and instead the constituent transition matrix is used, which is known from experiment. The integral equation approach is quite successful for studying elastic scattering where a one-body integral equation can be found by formulating an optical potential. For studying knockout and fragmentation reactions, the Eikonal approximation (Cucinotta *et al.*, 1989) is useful in order to reduce a many-body integral equation to a manageable form. The importance of final state interactions between projectile fragments suggests the use of a Faddeev type integral equation.

In the RMST, the infinite sum of meson exchange diagrams is written as an integral equation of the Bethe-Salpeter form (Maung *et al.*, 1996). The Bethe-Salpeter equation is reduced to a 3D form using a covariant 3D relativistic propagator. The propagator of Maung *et al.* (1996) is most useful for performing the 3D reduction, since it treats the target and projectile constituents

on an equal footing, avoiding non-physical singularities that occur with other propagators. The transition operator derived in the RMST is written as

$$(11) \quad T = K + KGT$$

where G is the Bethe-Salpeter propagator representing the two nuclei in intermediate states and the kernel K is the sum of all irreducible diagrams based on meson exchange theory for scattering of the projectile and target constituents. The kernel is decomposed into various terms corresponding to one meson exchange between constituents, two meson exchanges between constituents, two meson exchanges between more than one constituent,

$$(12) \quad K = K_1 + K_2 + K_{2X} + \dots$$

This infinite sum of irreducible diagrams is described by Maung *et al.* (1996). The 3D reduction of the RMST is found by introducing an approximate propagator g to obtain the coupled integral equations:

$$(13) \quad T = V + VgT$$

with

$$(14) \quad V = K + K(G - g)V$$

The 3D reduction is chosen to represent the best approximation to an exact propagator G . In application, the approximation $V \cong K_1$ is often evoked. The effects of nuclear clustering are considered in the MST by assuming the constituent interactions are those between clusters rather than the choice of nucleons (Maung *et al.*, 1996). The RMST with clusters involves complicated summations over irreducible diagrams among the cluster constituents. The choice of which cluster configuration is chosen is determined by reaction channel and nuclear structure considerations. The convergence of a cluster expansion series should be more rapid than the nucleon one when the kernel is known; however, more detailed bound state properties may be involved for performing such calculations.

The NRMST is obtained from eqs. (12)–(14) by approximating the full kernel by the leading order term corresponding to one-meson exchange diagrams and using a non-relativistic reduction of the 3D propagator g . The potential term is the sum of the interactions of the constituents

$$(15) \quad V = \sum_{j=1}^{A_p} \sum_{a=1}^{A_T} t_{aj}$$

and the non-relativistic propagator is given by

$$(16) \quad g_{NR} = (E - H_p - H_T)^{-1}$$

where H_p and H_T are the projectile and target internal Hamiltonians, respectively. The constituent interactions involve the full many-body problem as described by the integral equation

$$(17) \quad \mathbf{t}_{aj} = V_{aj} + V_{aj} g_{NR} \mathbf{t}_{aj}$$

where V is the nucleon-nucleon potential and the propagator includes the effects of nuclear binding. At high energies, the relative kinetic energy of the constituents is much larger than the binding energy, such that the propagator can be evaluated in the impulse approximation

$$(18) \quad g_o = (E - T_p - T_T)^{-1}$$

and the constituent interactions are replaced by the free interactions which are truly of the two-body form. For high-energy reactions, the scattering is often confined to the forward direction and the Eikonal approximation is accurate and to be used to reduce the scattering problem to a closed form expression. There are several approaches for deriving the Eikonal form of the MST. Here we continue our considerations of the nucleus-nucleus propagator and introduce the Eikonal propagator

$$(19) \quad g_{eik} = \left(\frac{\mathbf{k} \cdot (\mathbf{k} - \mathbf{k}')}{p_\alpha} \right) \delta(\mathbf{k} - \mathbf{k}')$$

The insertion of the Eikonal propagator into the MST allows for a summation of the series into a closed form expression. An alternative coupled-channels approach to the Eikonal approximation is considered by Cucinotta *et al.* (1989). Calculations using the Eikonal model are considered next.

The pre-fragment excitation spectrum following nucleon or alpha particle abrasion can be represented in terms of an impact parameter-dependent convolution of the pre-fragment excitation response for a transition of the pre-fragment core from state n to n' and the project fireball response (Cucinotta *et al.*, 1998b)

$$(20) \quad \frac{d\mathbf{S}}{d\mathbf{e}_{F*}} = \langle T | \int d^2q d^2b d^2b' e^{i\mathbf{q}(\mathbf{b}-\mathbf{b}')} P_{n,n'}(b, b') \Lambda_{n,n'}(q, b, b, E_{F*}) | T \rangle$$

where b (b') is the impact parameter, and q the momentum transfer. The abrasion response is defined as the interaction of the projectile fireball with the target after performing closure over the final fireball states

$$(21) \quad \Lambda_{n,n'}(b,b',E_f) = \int \frac{d\mathbf{k}_R}{(2\mathbf{p})^3} \langle R' | Q_{RT}^+(b') | R \rangle \langle R | Q_{RT}(b) | R' \rangle \mathbf{d}(E_i - E_f)$$

where the Q_{RT} represent the fireball-target profile operator, and k_R the projectile fireball momentum vector. The abrasion response represents a complicated many-body operator that is solved by approximation. The one-particle abrasion response has been evaluated using the shell model response functions (Cucinotta and Dubey, 1993). The pre-fragment excitation is described in terms of the transition matrix

$$(22) \quad P_{n,n'}(b,b',E_f) = \langle F_n^* | Q_{FT}^+(b') | F_{n'}^* \rangle \langle F_{n'}^* | Q_{FT}(b) | F_n^* \rangle$$

where matrix elements for the pre-fragment excitation are evaluated over the many-body profile operators, Q_{FT} . The model uses a convolution approach to derive the multi-knockout spectrum from the single-fragmentation term (Cucinotta and Dubey, 1994b).

The de-excitation of the pre-fragments in the QMSFRG model is described in a stochastic process using a Master equation for nuclear de-excitation by particle emission (Cucinotta and Wilson, 1996b). If $f^b(E,t)$ is the probability of finding the nuclei b at time t with excitation energy E_b and $P_k^b(E)$ the probability that the nuclei, b will emit ion k with energy E , then the Master equation is

$$(23) \quad \frac{df^b(E_b^*,t)}{dt} = \sum_j \int dE f^a(E_a^*,t) P_j^a(E) - \sum_k \int dE f^b(E_b^*,t) P_k^b(E)$$

In eq. (23), the first term on the right corresponds to gains by decays $a \rightarrow b+j$ and the second term from losses due to decays $b \rightarrow c+k$ where the j (or k) are light-particle emissions (n, p, d, t, h , or α). Eq. (23) is solved by iteration up to medium excitation energies (below 150 MeV) and by approximation for high excitation energies (Cucinotta *et al.* 1996b, 1998b). Important features of this solution is the correct description of the nuclear level-density including nuclear-shell effects at low-excitation energies, and the use of measured values for the nuclear masses. The fragmentation cross-section is then evaluated from eqs. (21)-(23) as

$$(24) \quad \mathbf{s}_F(A_F, Z_F) = \sum_{A_{F^*}, Z_{F^*}} \int dE_{F^*} \frac{d\mathbf{s}_{F^*}}{dE_{F^*}} f(A_{F^*}, Z_{F^*} \longrightarrow A_F, Z_F)$$

where $f(A_{F^*}, Z_{F^*} \longrightarrow A_F, Z_F)$ is the solution to eq. (23).

The QMSFRG theory reduces to the OPTFRG model (Townsend *et al.*, 1986) when energy conservation and nuclear medium effects are ignored and closure approximations on the pre-fragment and fireball states are made, and to the NUCFRG2 model (Wilson *et al.* 1995b) when the optical operators are expressed as volume overlaps functions. In both the OPTFRG and

NUCFRG2 models, all information on the pre-fragment excitation spectrum is lost and thus must be introduced in an *ad-hoc* manner independent of the collision model used to describe mass removal. Quantum interference effects in nuclear fragmentation can be ignored for heavy projectiles, but is important in the case of small projectile mass (Cucinotta *et al.*, 1992a) and also modifies nuclear absorption in quasi-inelastic scattering (Cucinotta *et al.*, 1992b, 1992c). For light particle fragmentation, we use the models of Cucinotta and co-workers described previously (Cucinotta, 1993, Cucinotta *et al.*, 1995b).

The iso-spin dependence in fragmentation cross-sections enters in several ways. First, the energy-dependent two-body nucleon interaction parameters are summed over the possible projectile and target nucleon scattering combinations. Second, the nuclear wave-functions will have a dependence on shell structure and the nuclear surface. The largest contribution to iso-spin effects occur in the nuclear ablation process (de-excitation) where the pre-fragments formed and their level spectra are greatly influenced by the projectile or pre-fragment iso-spin. Important aspects of the model include the use of Coulomb trajectories (Cucinotta *et al.*, 1997a) and in-medium nucleon-nucleon interaction (Tripathi *et al.*, 2000). Their effects on abrasion cross-sections are illustrated in **Figure 4** for ^{32}S fragmentation on aluminum targets at kinetic energy of 100 MeV/u. Clearly these aspects of the physics of fragmentation are important and their inclusion leads to improvements in the accuracy of fragmentation and absorption cross-sections databases.

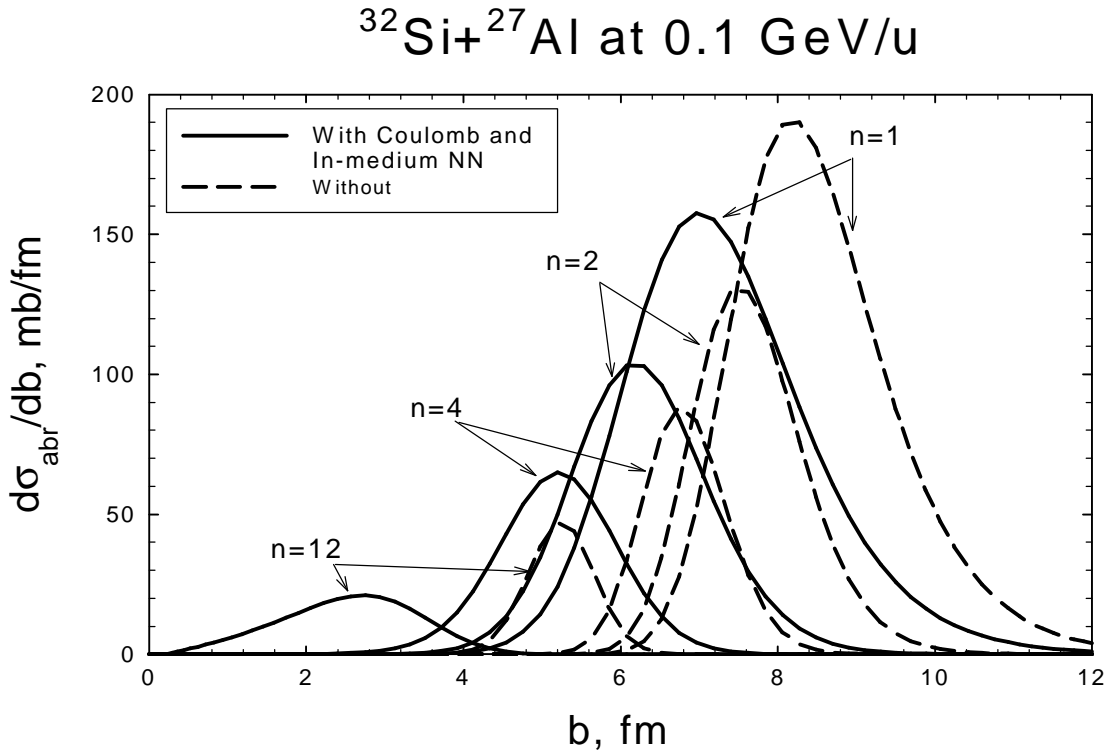


Figure 4: Abrasion cross-sections versus impact parameter for $n=1, 2, 4$, and 12 nucleon removal in ^{32}S fragmentation at 0.1 GeV/u on Al targets showing the corrections for Coulomb trajectories and the in-medium nucleon-nucleon interaction.

RESULTS

We first illustrate the accuracy of the QMSFRG model and the effects of iso-spin on fragmentation cross-sections. **Figures 5-16** show comparisons of the model to experimental data for the elemental distributions of fragments for several nuclei of similar mass number. All comparisons include the one- and two-nucleon removal cross-sections by electromagnetic dissociation (Norbury *et al.*, 1988). The iso-spin, $T_z=0$ nuclei display large odd-even effects, which are reduced for the $T_z > 0$ nuclei. The odd-even effects are present for all target nuclei, however are reduced for hydrogen targets due to the small abrasion probability for large mass removal on hydrogen. To see one of the errors that results from transporting ions using a reduced mass-grid, we compare fragmentation cross-sections for nearby projectiles where large differences in many of the production cross-sections occur for neighboring projectile nuclei. The model accurately reproduces the effects observed in the experiments. **Figures 17 and 18** show comparisons of QMSFRG predictions to experimental data for fragments from ^{40}Ar and ^{56}Fe projectiles. The results show good agreement between theory and experiments and indicate the larger number of isotopes that are produced during nuclear fragmentation. **Table 3** shows the isotopic table of 170 nuclei developed as a complete list of GCR primary and secondary nuclei to be used in GCR transport problems.

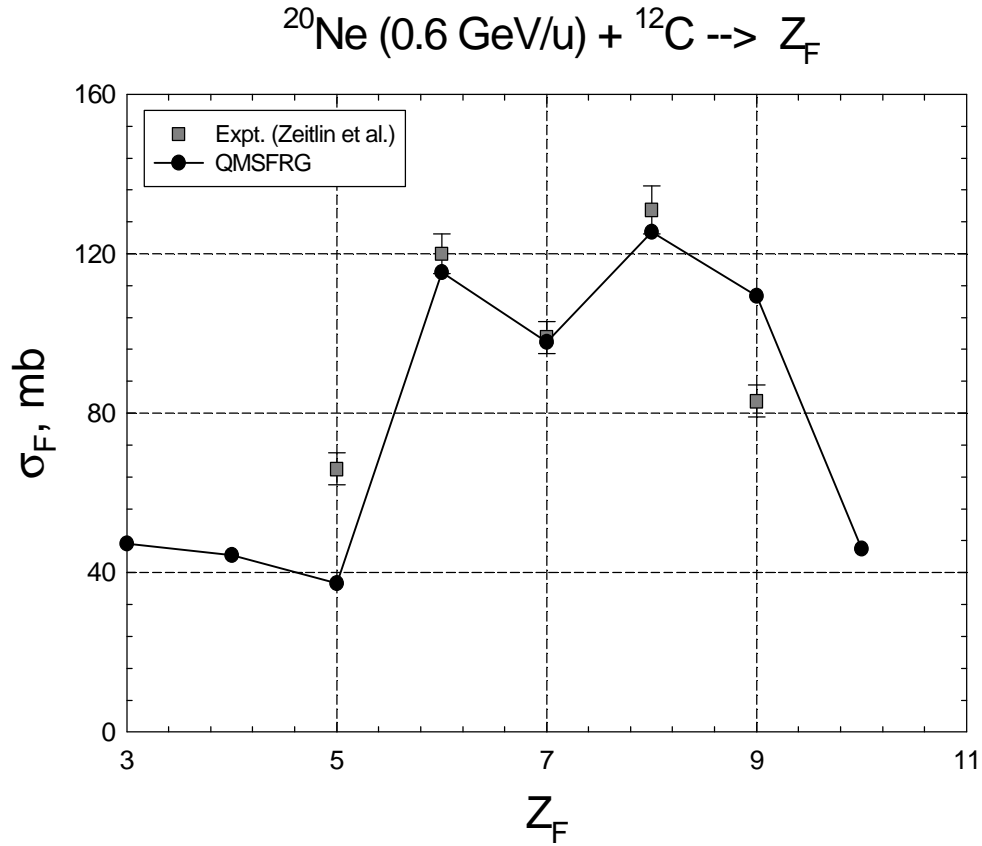


Figure 5: Comparisons of the QMSFRG model to experiment for elemental fragment distribution for ^{20}Ne on ^{12}C at 0.6 GeV/u. Experimental data from Zeitlin *et al.* (2001).

We have also listed in **Table 3** the mass excess (Audi and Wapstra, 1993), iso-spin, and half-life for the unstable nuclei along with the decay mode. This table of nuclei includes all nuclei of significant abundance with iso-spin $+3/2$ to -3 that appear in GCR transport problems. By contrast, early versions of the HZETRN code used a collapsed nuclear table. The expanded grid used here will allow for improved description of the physics, and to discuss many applications where unstable nuclei are central to understanding. Also listed in the first column of **Table 3** is the index scheme that is used in the HZETRN code, which is used to label the shielding-depth and energy-dependent fluence matrix. The index for the nuclei are ordered by increasing mass number, A , followed by charge number, Z , for a given A .

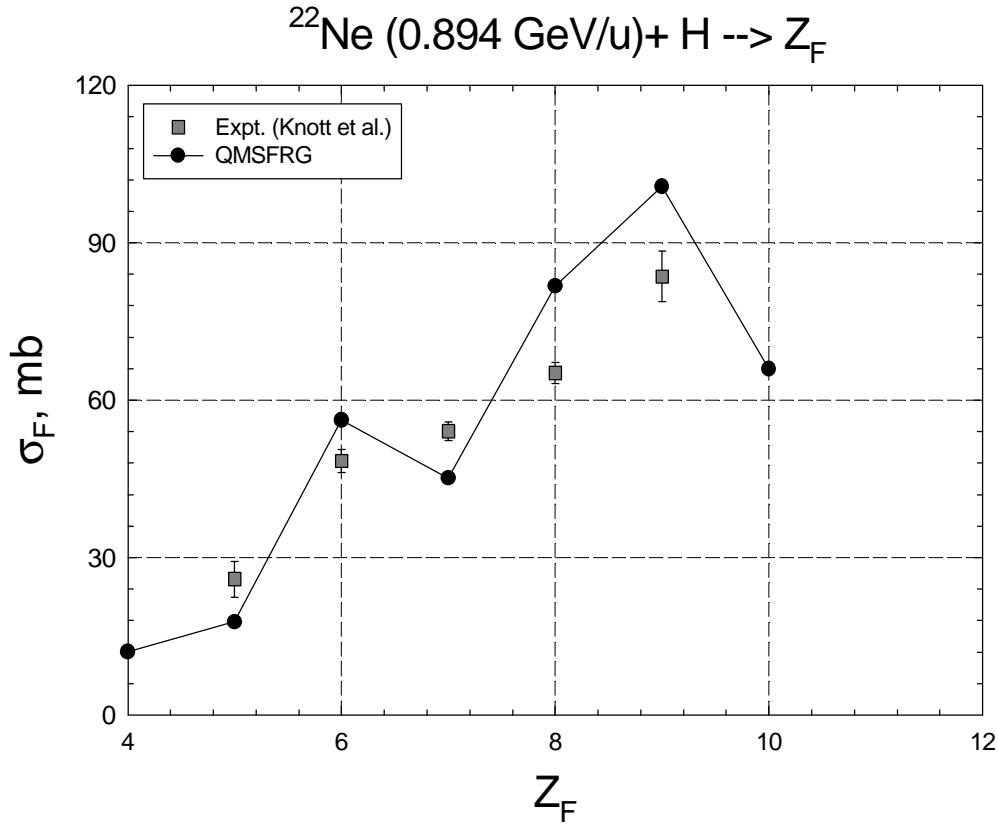


Figure 6: Comparisons of the QMSFRG model to experiment for the elemental fragment distribution for ^{22}Ne on ^1H at 0.894 GeV/u. Experimental data from Knott *et al.* (1996).

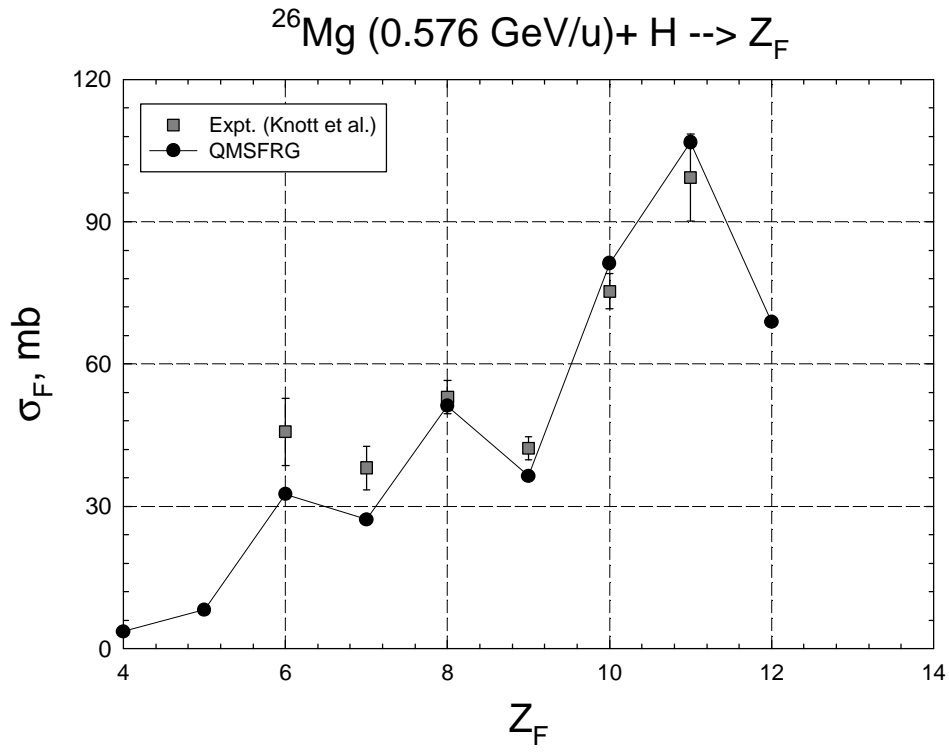


Figure 7: Comparisons of the QMSFRG model to experiment for elemental fragment distribution for ^{26}Mg on ^1H at 0.576 GeV/u. Experimental data from Knott *et al.* (1996).

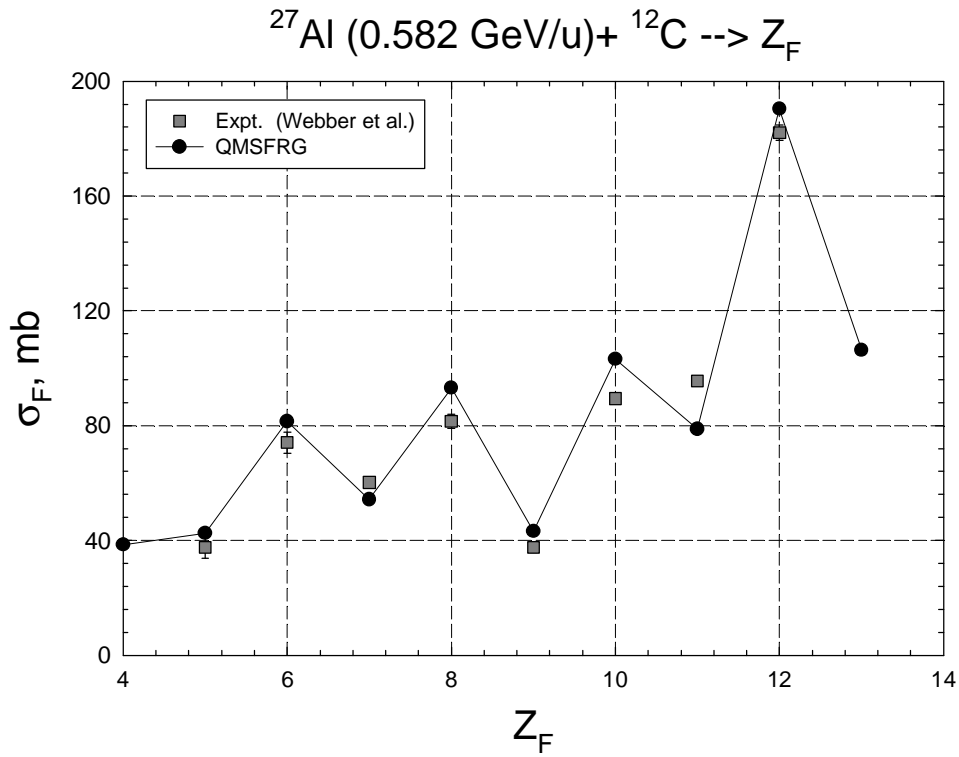


Figure 8: Comparisons of the QMSFRG model to experiment for elemental fragment distribution for ^{27}Al on ^{12}C at 0.582 GeV/u. Experimental data from Webber *et al.* (1990).

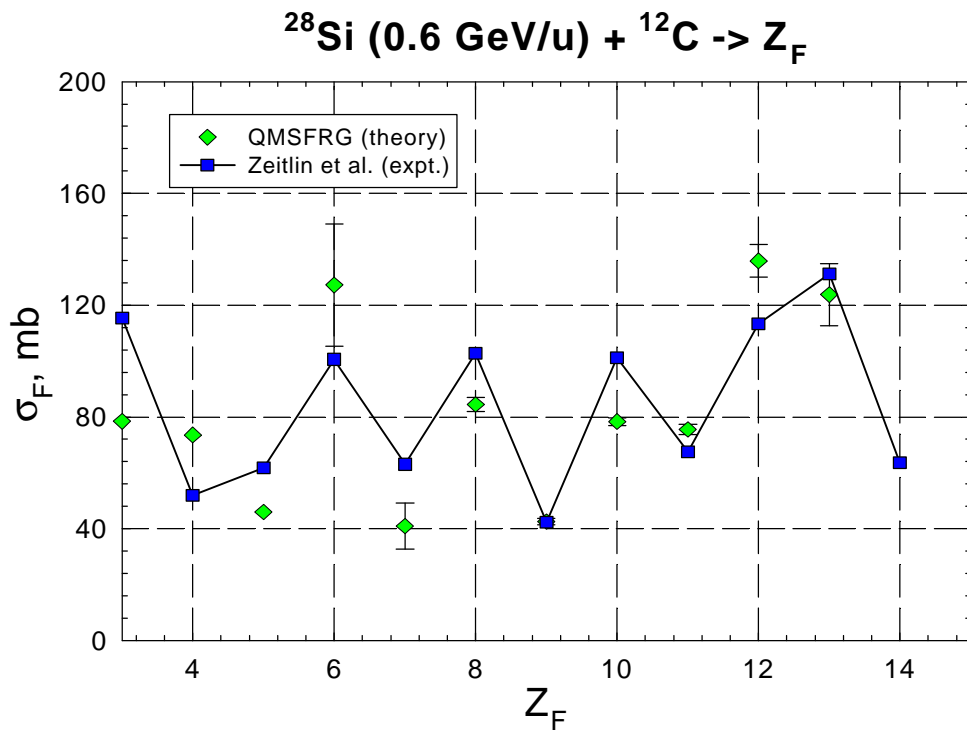


Figure 9: Comparisons of the QMSFRG model to experiment for elemental fragment distribution for ^{28}Si on ^{12}C at 0.6 GeV/u. Experimental data of Zeitlin *et al.* (2002).

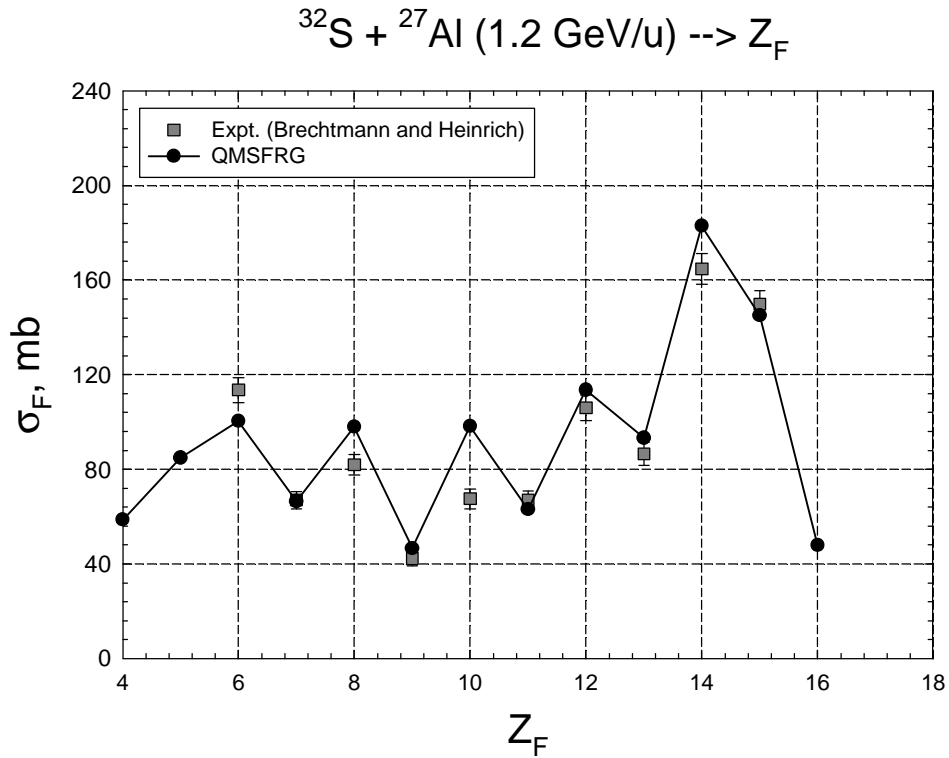


Figure 10: Comparisons of the QMSFRG model to experiment for elemental fragment distribution for ^{32}S on ^{27}Al at 1.2 GeV/u. Experimental data of Brechtmann *et al.* (1988).

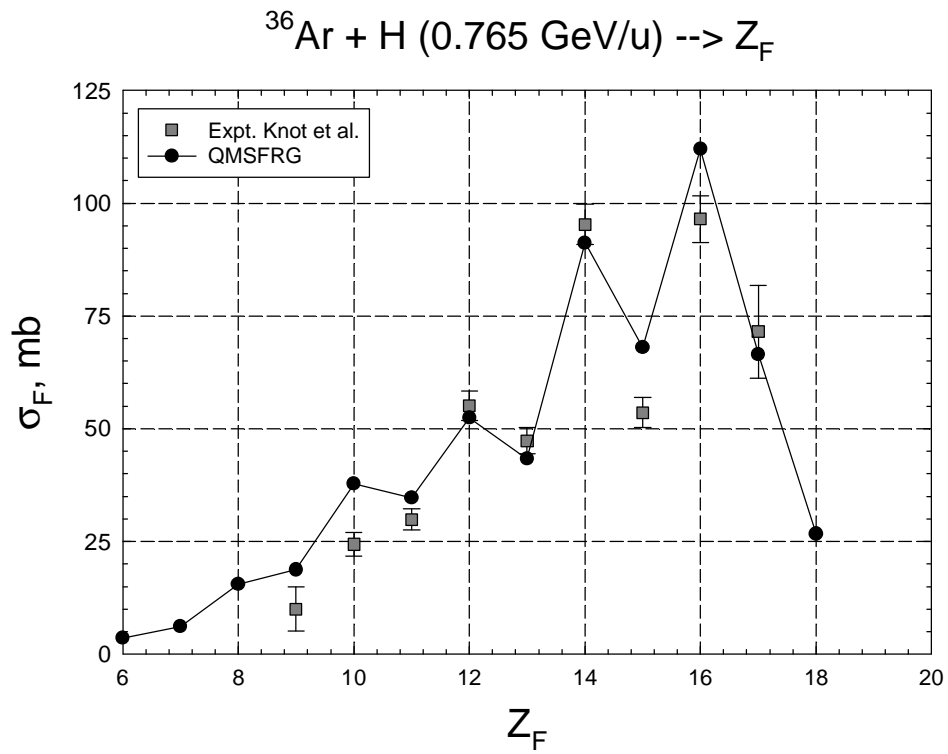


Figure 11: Comparisons of the QMSFRG model to experiment for elemental fragment distribution for ^{36}Ar on ^1H at 0.765 GeV/u. Experimental data from Knott *et al.* (1996).

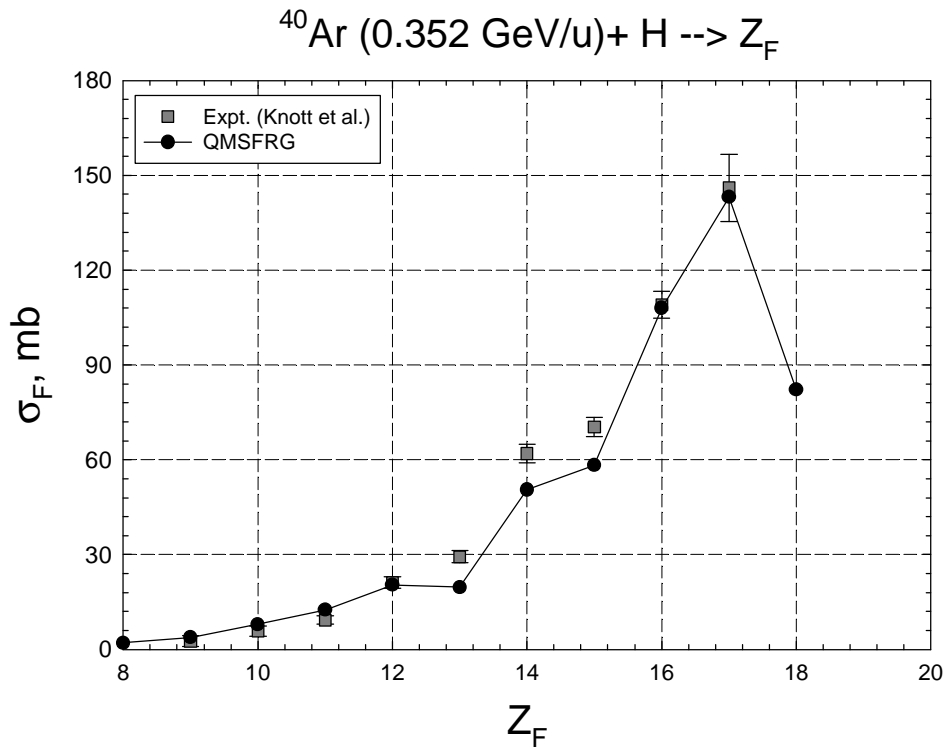


Figure 12: Comparisons of the QMSFRG model to experiment for elemental fragment distribution for ^{40}Ar on ^1H at 0.352 GeV/u. Experimental data from Knott *et al.* (1996).

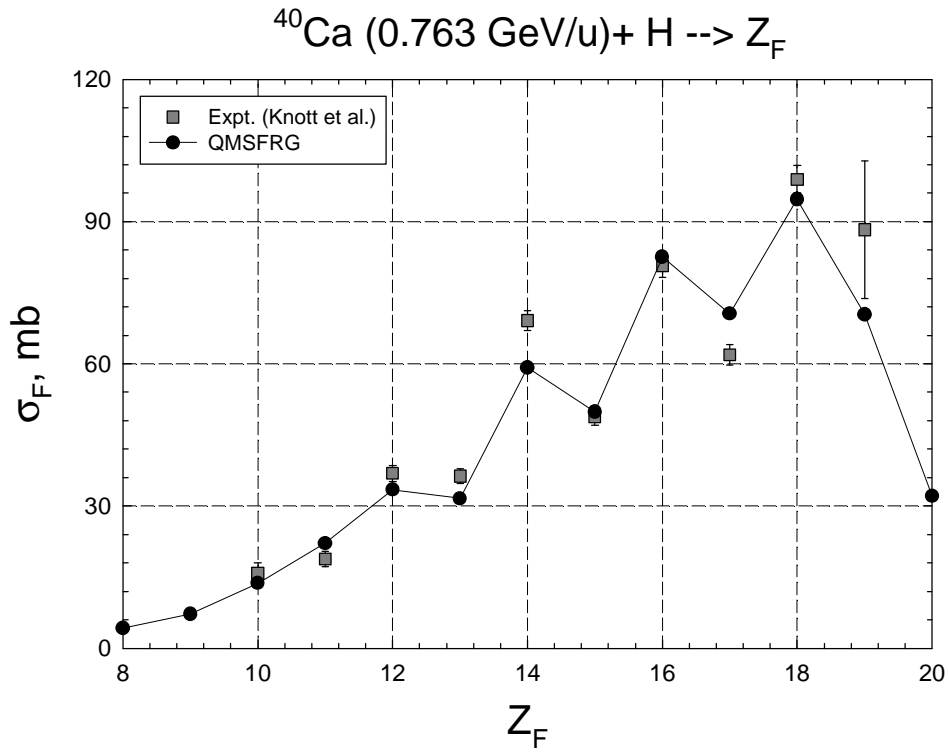


Figure 13: Comparisons of the QMSFRG model to experiment for elemental fragment distribution for ^{40}Ca on ^{12}C at 0.763 GeV/u. Experimental data from Knott *et al.* (1996).

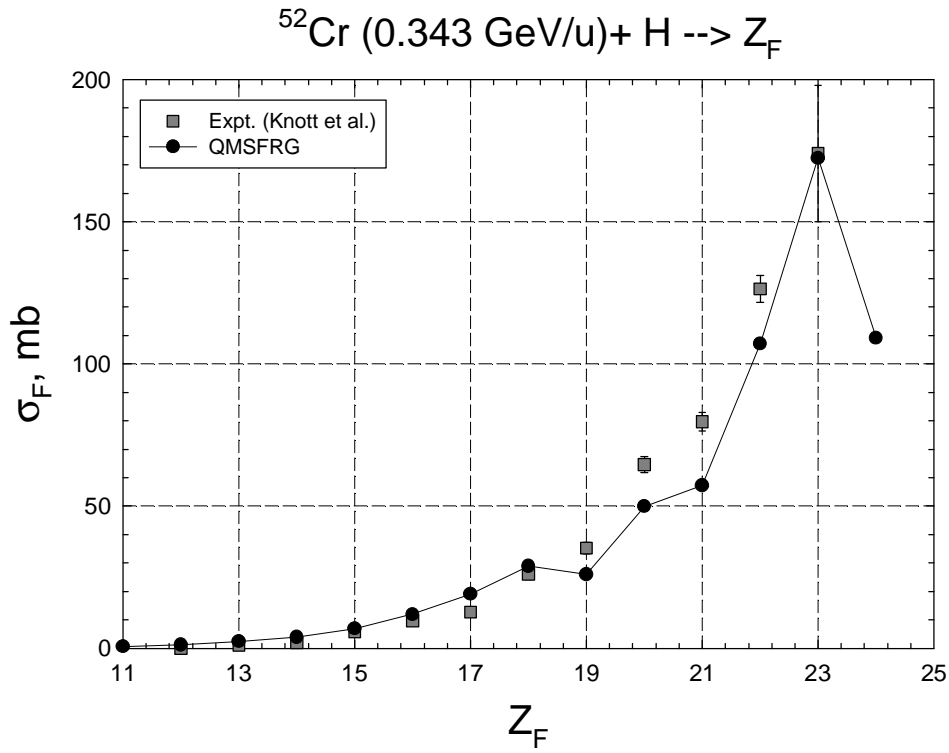


Figure 14: Comparisons of the QMSFRG model to experiment for elemental fragment distribution for ^{52}Cr on ^1H at 0.338 GeV/u. Experimental data from Knott *et al.* (1996).

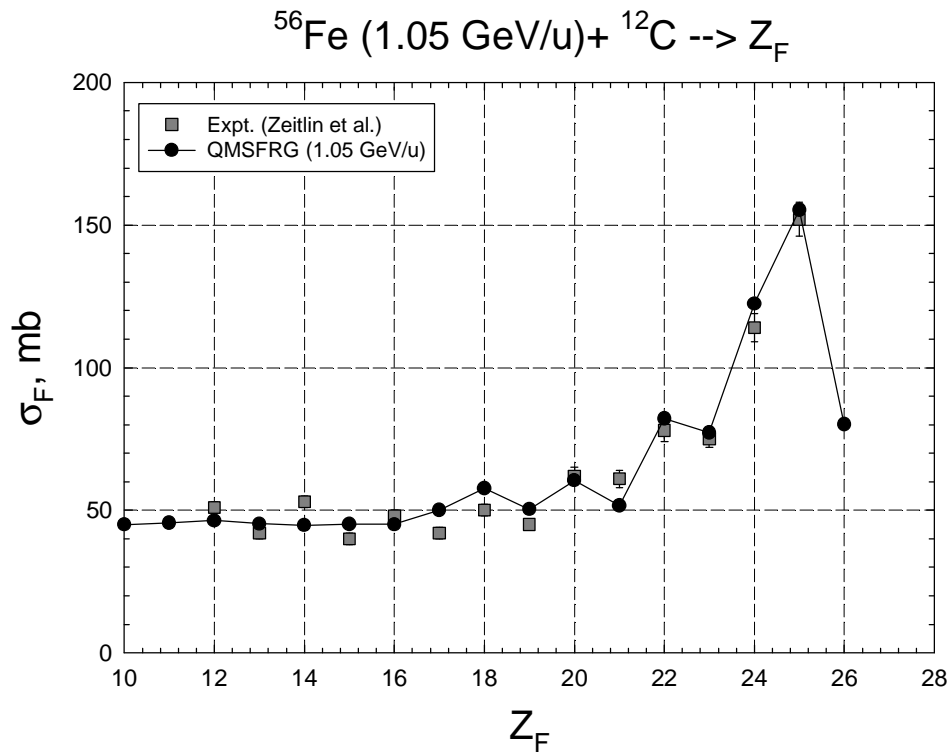


Figure 15: Comparisons of the QMSFRG model to experiment for elemental fragment distribution for ^{56}Fe on ^{12}C at 1.05 GeV/u. Experimental data of Zeitlin *et al.* (1997).

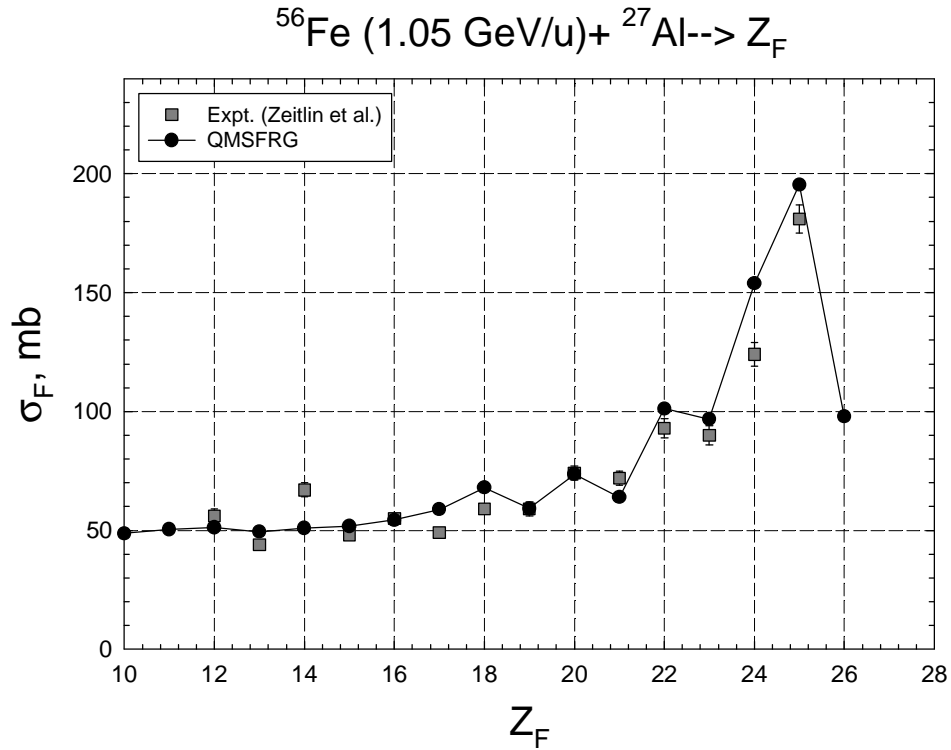


Figure 16: Comparisons of the QMSFRG model to experiment for elemental fragment distribution for ^{56}Fe on ^{27}Al at 1.05 GeV/u. Experimental data of Zeitlin *et al.* (1997).

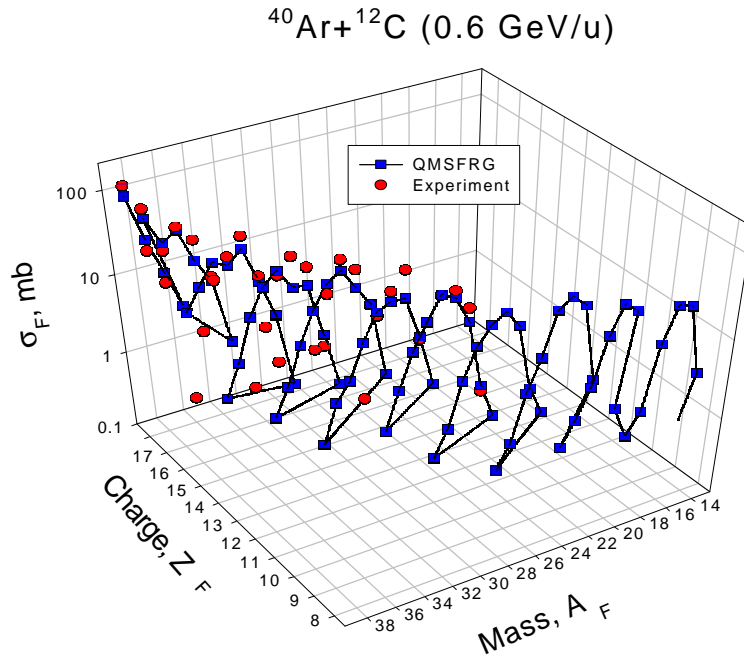


Figure 17: Comparisons of the QMSFRG model to experiment for the isotopic distribution of fragments for ^{40}Ar on ^{12}C at 0.6 GeV/u. Experimental data from Webber *et al.* (1990b).

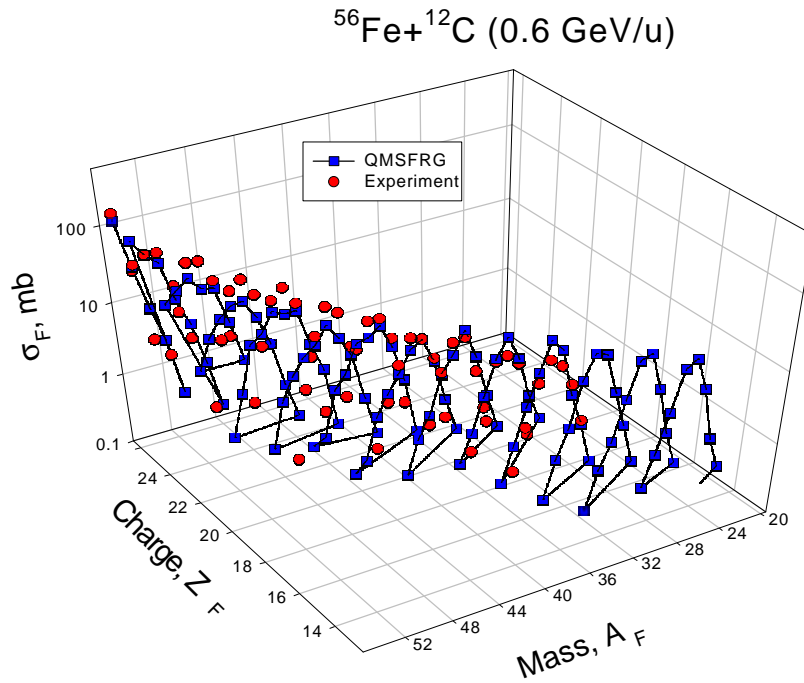


Figure 18: Comparisons of the QMSFRG model to experiment for the isotopic distribution of fragments for ^{56}Fe on ^{12}C interactions at 0.6 GeV/u. Experimental data from Webber *et al.* (1990b).

The GCR nuclei are completely stripped and therefore the decay mode and half-life for unstable nuclei could be differential from those observed in laboratories on Earth. Garcia-Munoz *et al.* (1987) has noted the following differences: 1) electron capture branches, which are inactive for GCR nuclei relative to β -decay, 2) for non-stripped nuclei there will be two S-shell electrons that participate in electron capture that will not be available in the decay of GCR nuclei, and 3) changes in screening effects. They have made estimates of the elongation of the half-time for fully stripped nuclei due to these processes, which indicate an approximate doubling of the decay time observed for laboratory nuclei that normally decay by electron capture. Since these decay times are much longer than the transit time of nuclei in shielding they are not considered here. However, it will be useful in the future to further consider these processes when studying the effects of stopping GCR nuclei on planetary atmospheres or surfaces and in tissues.

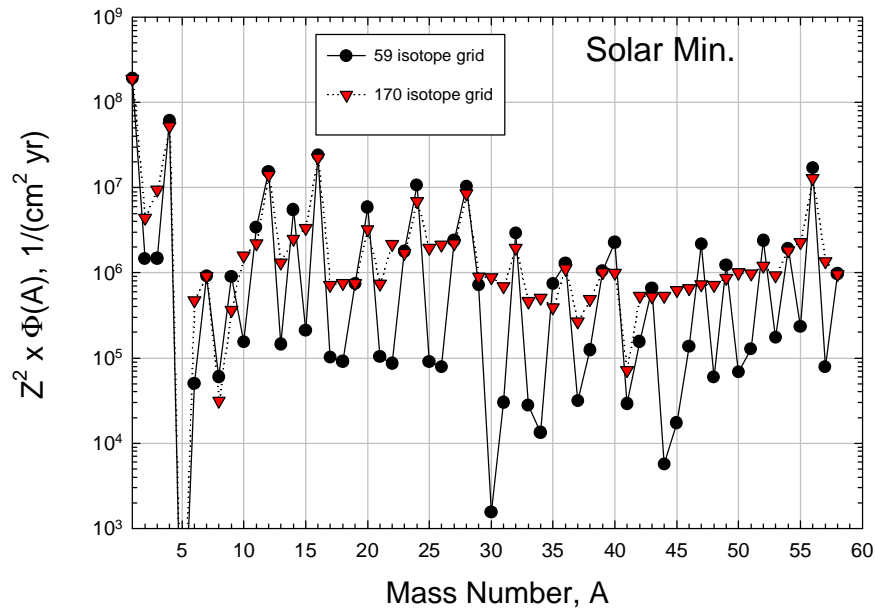


Figure 19: Comparisons of results from the HZETRN code for the mass fluence distribution behind 5 g/cm² of aluminum shielding for solar minimum conditions comparing transport with the reduced 59-isotope grid to transport with a full 170-isotope grid.

Figure 19 shows results from the HZETRN code at solar minimum ($\Phi=428$ MV) behind 5 g/cm² of aluminum shielding. Comparison of the mass-flux spectra for a 59-isotope grid and the 170-isotope grid are shown. The 170-isotope grid was developed by considering the fragmentation cross-sections for a large number of GCR primary nuclei and dominant fragments in several materials. In **Figure 19** we have scaled the fluence by the square of the ion charge as a measure of the ionization power of each mass group. Large differences are seen for many

nuclei. **Figure 20** shows the percent error in the mass-fluence spectra resulting from the use of the reduced isotope grid for shielding depths of 5 and 20 g/cm² of aluminum. Errors greater than 100% are seen for many nuclei, however in most cases such large errors only occur for the less abundant nuclei. The probability of biological effects is expected to increase in a manner proportional to Z^2 for a given energy, and the elemental-fluence distribution may be a sufficient test of transport models for supporting exploration studies. In **Figure 21**, we show a similar comparison to that of **Figure 20**, however here for the elemental-fluence spectra. The errors are indeed less substantial than those of the mass-fluence spectra, yet are larger than 10% in several cases. Similar comparisons near solar maximum conditions ($\Phi=1050$ MV) are shown in **Figures 22 and 23**. **Table 4** shows results for the elemental and neutron excess dependence of the point dose equivalent behind aluminum shielding. The $Y<-1$ nuclei are not significant, while all other cases make important contributions to the dose equivalent. **Table 5** shows the fluence at several depths for several of the cosmic-ray clock nuclei and other less abundant nuclei of interest for scientific studies.

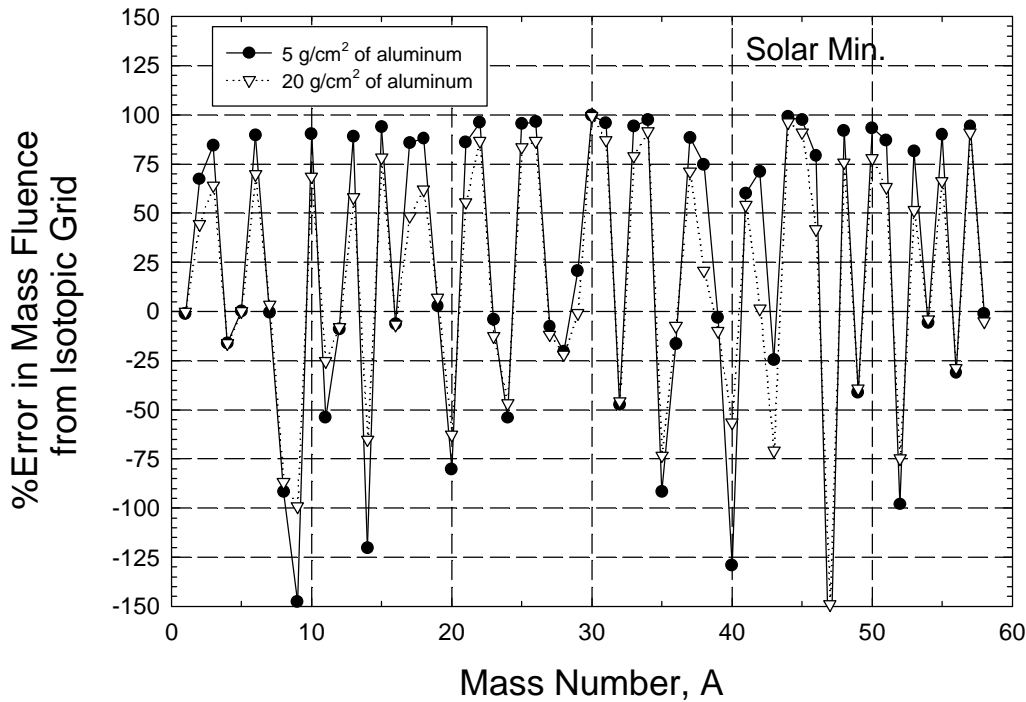


Figure 20: Comparisons of the error that results from the HZETRN code for the mass fluence distribution near solar minimum when using a reduced 59-isotope grid compared to transport with a 170-isotope grid.

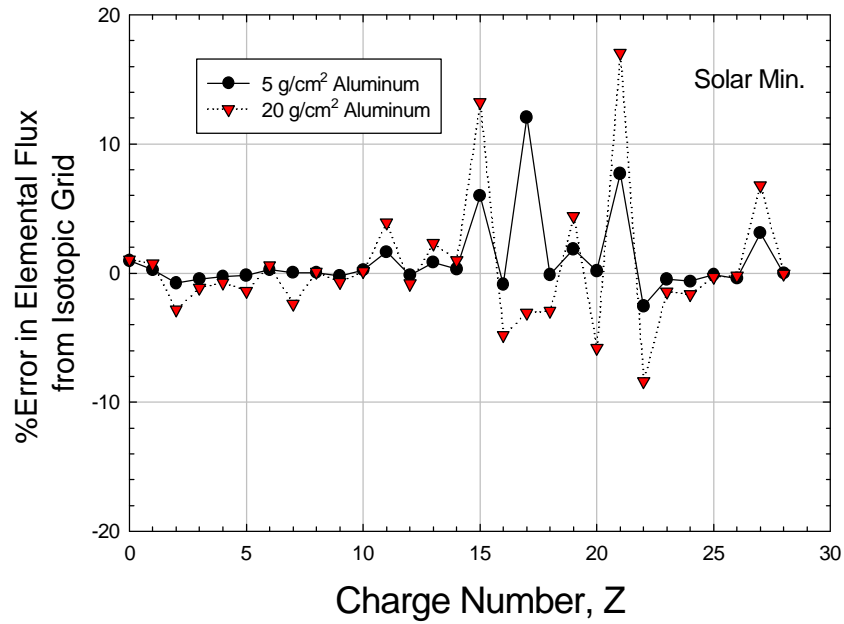


Figure 21: Comparisons of the error that results from the HZETRN code for the elemental fluence distribution near solar minimum when using a reduced 59-isotope grid compared to transport with a 170-isotope grid.

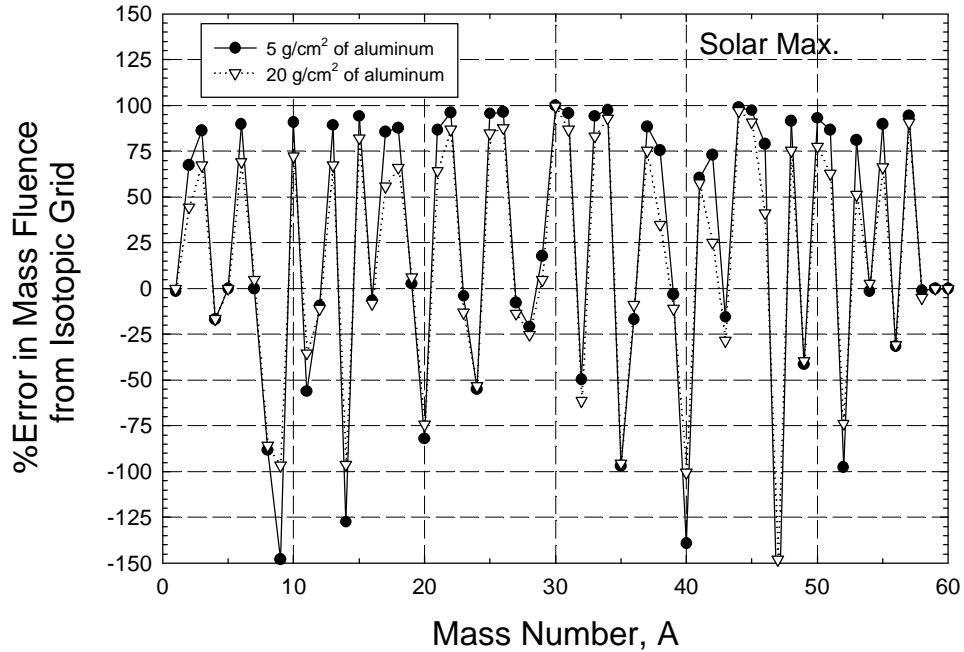


Figure 22: Comparisons of the error that results from the HZETRN code for the mass fluence distribution near solar maximum when using a reduced 59-isotope grid compared to transport with a 170-isotope grid.

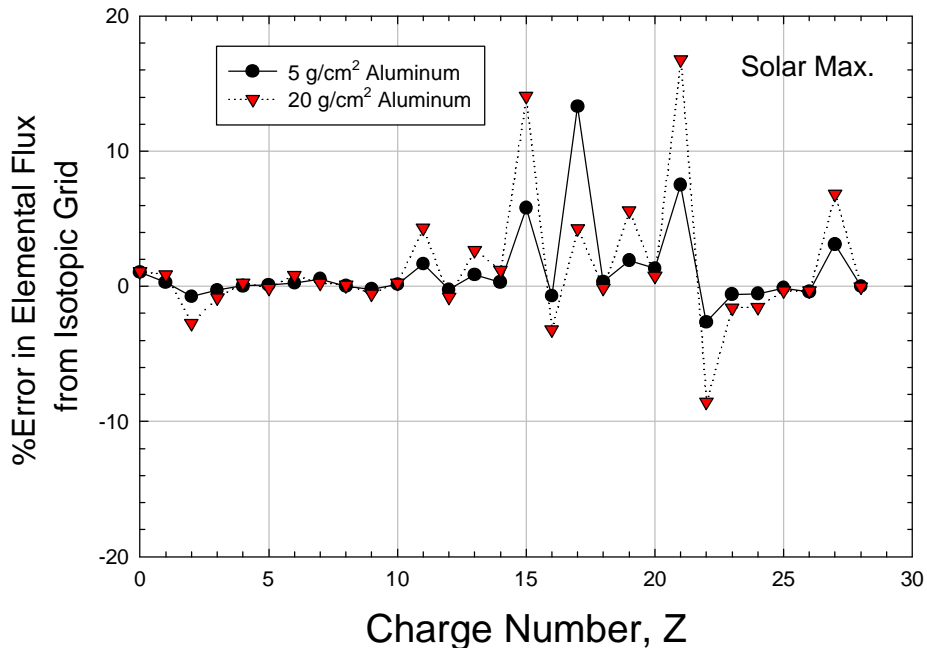


Figure 23: Comparisons of the error that results from the HZETRN code for the elemental fluence distribution near solar maximum when using a reduced 59-isotope grid compared to transport with a 170-isotope grid.

DISCUSSION

It has been recognized for many years that—for the description of GCR transport in shielding—theoretical models and experimental data describing the nuclear interactions and propagation of protons, heavy ions, and their secondaries leading to accurate and computational efficient transport codes are needed. In the last 25 years, such descriptions have improved dramatically. Major milestones have included developing an accurate free space GCR model (Badhwar and O'Neill, 1992), the HZETRN code (Wilson, 1977; Wilson, et al., 1990); measuring a significant number of fragmentation cross-sections (Brechtmann and Heinreich, 1988; Webber, *et al.*, 1990b; Knott, *et al.* 1996, 1997; and Zeitlin *et al.*, 1997, 2001, 2002), and developing an accurate nuclear fragmentation model (Cucinotta, *et al.*, 1998a). Laboratory (Schimmerling *et al.*, 1989) and spaceflight (Badhwar and Cucinotta, 2000) validation data have also become available during this time period. The implementation of heavy ion transport models has progressed from models that lacked unitarity (Letaw *et al.*, 1983) to the current fully energy-dependent models with accurate absorption cross-sections (Shinn *et al.*, 1994; Wilson *et al.*, 1993; Cucinotta, 1993). Future work may still be required for light-particle transport (n , p , d , t , h , α , and mesons and their

decay products), including establishing production cross-section models and data, and understanding the role of angular deflections, which are expected to be more important for heavy ion transport. However, the heavy ion problem is in much better shape, with many of the remaining tasks implementation issues. One exception may be improvements in fragmentation cross-sections and laboratory validation for the $Z=1$ to 5 nuclei produced from the heavier projectile nuclei ($Z>10$).

The present paper addressed two implementation tasks: the use of a free-space GCR model, which includes the isotopic composition of the primaries, and the extension of the HZETRN code to a complete isotope grid. The problem of the isotopic distribution of the primary GCR and their modulation during the solar cycle has been treated in a parametric way in this paper. In this approach, we maintain the accuracy of the GCR modulation model for the GCR elemental spectra from Badhwar and O'Neill (1992), however redistribute the fluence of each element amongst its isotopes using estimates from satellite data. Although performing more extensive fits to satellite data could make improvements, the coupling of the HZETRN code to the Leaky Box Model is suggested as the solution approach to this problem. Using the complete isotope grid of nuclei will allow HZETRN applications on the study of the so-called cosmic ray "clocks" with lifetimes similar to the time spent by GCR nuclei in the galaxy (~ 1 M-yr) as well as studies of signature nuclei from the decay of GCR nuclei in the atmosphere or on planetary surfaces where lifetimes on the order of a few to several thousand years will be important. Because the use of a reduced grid leads to error and there are no practical limitations in using a complete isotope grid at this time, we recommend it be used when initiatives to design space exploration vehicles begin. Future tasks that remain are to implement physical models of the GCR isotopic environment and to continue to refine the QMSFRG model, including comparisons to new fragmentation data as they become available. For the many deformed and highly deformed projectile nuclei considered herein, methods to consider this deformation in the abrasion process are needed. Another consideration for the future is the decay of radioactive isotopes produced as GCR secondaries in planetary atmospheres, shielding materials, or tissue. Such tasks are being considered by the present authors and will be reported elsewhere.

ACKNOWLEDGMENTS

The authors express their sincere appreciation for the partial funding support received from the projects: MARIE (Martian Radiation Environment Experiment on 2001 Mars Odyssey) and NEXT (NASA Exploration Team), project funding numbers 111-40-10 and 732-50.

REFERENCES

- Anonymous, Strategic Space Radiation Health Program Plan, NASA Office of Life Sciences and Microgravity Applications, Washington D.C. (1998).
- G. Audi, and A.H. Wapstra, The 1993 Atomic Mass Evaluation (I) Atomic Mass Table. *Nucl. Phys.* **A565**, 1-65 (1993).
- G.D. Badhwar, and P.M O'Neill, An Improved Model of GCR for Space Exploration Missions. *Nucl. Tracks Radiat. Meas.* **20**, 403-410 (1992).
- G.D. Badhwar, and F.A. Cucinotta, A Comparison on Depth Dependence of Dose and Linear Energy Transfer Spectra in Aluminum and Polyethylene. *Radiat. Res.* **153**, 1-8 (2000).
- G.D. Badhwar, W. Atwell, F. F. Badavi, T. C. Yang, and T. F. Cleghorn, Space Radiation Absorbed Dose Distribution in a Human Phantom, *Radiat. Res.* **157**, 76-91 (2002).
- G.D. Badhwar, MArtian Radiation EnvIronment Experiment (MARIE), Special Issue on *2001 Mars Odyssey*, NASA-JPL Publication, in press (2003).
- C. Brechtmann, and W. Heinrich, Fragmentation Cross-sections of ^{32}S at 0.7, 1.2, and 200 GeV/nucleon. *Z.Phys.* **A331**, 463-472 (1988).
- M. Cloudsley, J.W. Wilson, M.H.Y. Kim, R.C. Singleterry, R.K. Tripathi, J.H. Heinbockel, F.F. Badavi, and J.L. Shinn, Neutron Environments on the Martian Surface. *Phys. Medica* **XVII** 94-96 (2001).
- F.A. Cucinotta, G.S. Khandelwal, L.W. Townsend, and J.W. Wilson, Correlations in α - α Scattering and Semi-Classical Optical Models. *Phys. Lett.* **B223**, 127-132 (1989).
- F.A. Cucinotta, L.W. Townsend, and J.W. Wilson, Production of ^3H at Large Momentum in α - ^{12}C Collisions at 2 A GeV. *Phys. Lett.* **B282**, 1-6 (1992a).
- F.A. Cucinotta, L.W. Townsend, and J. W. Wilson, Inclusive Inelastic Scattering of Heavy Ions in the Independent Particle Model. *J. Phys. G: Nucl. Part. Phys.* **18**, 889-901 (1992b).
- F. A. Cucinotta, L. W. Townsend, and J. W. Wilson, Multiple Scattering Effects in Quasi-Elastic α - ^4He Scattering. *Phys. Rev. C* **46**, 1451-1456 (1992c).
- F.A. Cucinotta, Calculations of Cosmic-Ray Helium Transport in Shielding Materials. NASA TP-3354 (1993a).
- F.A. Cucinotta and R.R. Dubey, Final State Interactions and Inclusive Nuclear Collisions. NASA TP-3533 (1993b).
- F.A. Cucinotta, J.W. Wilson, and F.F. Badavi, Extension of BRYNTRN Code to Monoenergetic Light Ion Beams. NASA TP-3472 (1994a).

- F.A. Cucinotta, and R. R. Dubey, Alpha Cluster Description of Excitation Energies in ^{12}C (^{12}C , 3 **a**) X at 2.1 GeV. *Phys. Rev.* **C50**, 979-984 (1994b).
- F.A. Cucinotta, Forward Production of Protons in Relativistic ^{12}C -nucleus Collisions. *J. Phys. G: Nucl. Part. Phys.* **20**, 1803-1815 (1994c).
- F.A. Cucinotta, and J.W. Wilson, Initiation-Promotion Model of Tumor Prevalence in Mice From Space Radiation Exposure. *Radiat. Environ. Biophys.* **34**, 145-149 (1995a).
- F.A. Cucinotta, Townsend, L. W., J.W. Wilson, J.L. Shinn, G.D. Badhwar, and R. R. Dubey, Light Ion Components of the Galactic Cosmic Rays: Nuclear Interactions and Transport. *Adv. in Space Res.* **17**, 77-86 (1995b).
- F.A. Cucinotta, J.W. Wilson, M.R. Shavers, and R. Katz, The Effects of Track Structure and Cell Inactivation on the Calculation of Heavy Ion Mutation Rates in Mammalian Cells, *Inter. J. Radiat. Biol.* **69**, 593-600 (1996a).
- F.A. Cucinotta, and J.W. Wilson, Study of Analytical Statistical Model for Decay of Light and Medium Mass Nuclei in Nuclear Fragmentation. NASA TP-3594 (1996b).
- F.A. Cucinotta, et al., Computational Procedures and Data-Base Development. In: NASA Workshop on Shielding Strategies for Human Space Exploration. Eds. Wilson J.W., Miller J., Konradi A., and Cucinotta F.A., NASA CP-3360 (1997a).
- F.A. Cucinotta, J.W. Wilson, and L.W. Townsend, Abrasion-Ablation Model for Neutron Production in Heavy Ion Collisions. *Nucl. Phys. A.* **619**, 202-212 (1997b).
- F.A. Cucinotta, J.W. Wilson, J.L. Shinn, and R.K. Tripathi, Assessment and Requirements of Nuclear Reaction Data Bases for GCR Transport in the Atmosphere and Structures. *Adv. in Space Res.* **21**, 1753-1762 (1998a).
- F.A. Cucinotta, J.W. Wilson, R.K. Tripathi, and L.W. Townsend, Microscopic Fragmentation Model for Galactic Cosmic Ray Studies. *Adv. in Space Res.* **22**, 533-537 (1998b).
- F.A. Cucinotta, J.W. Wilson, J.R. Williams, and J.F. Dicello, Analysis of Mir-18 Results For Physical and Biological Dosimetry: Radiation Shielding Effectiveness in LEO. *Radiat. Meas.* **132**, 181-191 (2000).
- F.A. Cucinotta, W. Schimmerling, J.W. Wilson, L.E. Peterson, G. Badhwar, P. Saganti, and J.F. Dicello, Space Radiation Cancer Risks And Uncertainties For Mars Missions, *Radiat. Res.* **156**, 682-688 (2001).
- F.A. Cucinotta, Isotopic Effects in Nuclear Fragmentation and GCR Transport Problems. Proceedings of Shielding Technology Workshop, Hampton VA (2002).
- B. D. Fields, K. A. Olive, and D. N. Schramm, Cosmic Ray Models for Early Galactic Lithium, Beryllium and Boron Production, Fermilab-Pub-94/010-A (1994).
- M. Garcis-Munoz, J.A. Simpson, T.G. Guzik, J.P. Wefel, and S.H. Margolis, Cosmic-ray Propagation in the Galaxy and in the Heliosphere: The Path-Length Distribution at Low Energy. *Astrophys. J. Suppl.* **64**, 269-304 (1987).

- A. Hesse, *et al.*, The Isotopic Composition of Silicon and Iron in the Cosmic Radiation as Measured by the ALICE Experiment. 22nd International Conference, The Dublin Institute for Advanced Studies, Dublin, 596-599 (1991).
- M. Kim, J.W. Wilson, R.L. Kiefer, and S.A. Thibeault, Effects of Isotope Selection on Solution Convergence in HZE Transport. NASA TP-3445 (1994).
- C.N. Knott, *et al.*, Interactions of Relativistic Neon to Nickel Projectiles in Hydrogen, Elemental Production Cross-sections. *Phys. Rev.* **C53**, 347-357 (1996).
- C.N. Knott, *et al.*, Interactions of Relativistic ³⁶Ar and ⁴⁰Ar Nuclei in Hydrogen: Isotopic Production Cross-sections. *Physical Review* **C56**, 398-406 (1997).
- J. Letaw, C.H. Tsao, and R. Silberberg, Matrix Methods of Cosmic Ray Propagation. Composition and Origin of Cosmic Rays, Maurice M. Shapiro, ed., D. Reidel Publ. Co, 337-342 (1983).
- A. Lukasiak, P. Ferrando, F.B. McDonald, and W.R. Webber, Cosmic Ray Composition of $6 < Z < 8$ Nuclei in the Energy Range 50-150 MeV/n by the Voyager Spacecraft during the Solar Minimum and Maximum Periods. 23rd International Cosmic Ray Conference, La Jolla , USA, 539-542 (1993).
- A. Lukasiak, F.B. McDonald, W.R. Webber, and P. Ferrando, Voyager Measurements of the Isotopic Composition of Sc, Ti, V, Cr, Mn, and Fe Nuclei. 24th International Conference Ray Conference, Vol. 2, 576-579 (1995).
- K.M. Maung, John W. Norbury and David E. Kahana, Proportionally off-mass-shell equation for unequal mass systems, *J. Phys. G: Nucl. Part. Phys.* **22** No 3, 315-320 (1996).
- J.W. Norbury, F.A. Cucinotta, L.W. Townsend, and F.F. Badavi, Parameterized Cross Sections in Heavy-Ion Collisions. *Nucl. Instrum. Meth. Phys. Res.* **B31**, 535-537 (1988).
- E.N. Parker, The Passage of Energetic Charged Particles Through Interplanetary Space. *Planet Space Sci.* **13**, 9-49 (1965).
- W. Schimmerling, J. Miller, M. Wong, M. Rapkin, J. Howard, H.G. Spieler, and J. V. Blair, The Fragmentation of 670A MeV Neon-20 as a Function of Depth in Water. *Radiat. Res.* **120**, 36-51 (1989).
- J.L. Shinn, J.W. Wilson, F.F. Badavi, Fully-Energy Dependent HZETRN. NASA TP-3243 (1994).
- L.W. Townsend, J.W. Wilson, F.A. Cucinotta, and J.W. Norbury, Comparison of Optical Model Differences in Heavy Ion Fragmentation: Optical Versus Geometric. *Phys. Rev.* **C34**, 1491-1495 (1986).
- R.K. Tripathi, J.W. Wilson, and F.A. Cucinotta, Medium Modified Two-Body Scattering Amplitude from Proton-Nucleus Total Cross-Sections. *Nucl. Instrum. Meth. Phys. Res* **B173**, 391-396 (2001).
- W.R. Webber, J.C. Kish, and D.A. Schrier, Cosmic Ray Isotope Measurements with a New Cerenkov Total Energy Telescope. 19th International Cosmic Ray Conference, La Jolla , USA, 88-95 (1985).

- W.R. Webber, A. Southoul, P. Ferrando, and M. Gupta, The Source Charge and Isotropic Abundances of Cosmic Rays with $Z=9-16$: A Study Using New Fragmentation Cross-Sections. *The Astrophys. J.* **348**, 611-620 (1990a).
- W.R. Webber, J.C. Kish, and D.A. Schrier, Individual Isotopic Fragmentation Cross-Sections of Relativistic Nuclei in Hydrogen, Helium and Carbon Targets, *Phys. Rev.* **C41**, 547 (1990b).
- M.E. Wiedenback and D.E. Greiner, High-Resolution Observations of the Isotopic Composition of Carbon And Silicon in the Galactic Cosmic Rays. *The Astrophys. J.* **247** L119-L122 (1981).
- M.E. Wiedenback, The Isotopic Composition on Cosmic Ray Chlorine, 19th International Cosmic Ray Conference, La Jolla , USA, 1985, 84-87 (1985).
- J.W. Wilson, Analysis of Theory of High-Energy Transport. NASA TN D-8381 (1977).
- J.W. Wilson and F.F. Badavi, Methods of Galactic Heavy Ion Transport. *Radiat. Res.* **108**, 231-237 (1986).
- J.W. Wilson, L.W. Townsend, W. Schimmerling, G.S. Khandelwal, F. Khan, J.E. Nealy, F.A. Cucinotta, L.C. Simonsen, J.L. Shinn, and J.W. Norbury, Transport Methods and Interactions for Space Radiations. NASA RP-1257 (1991).
- J.W. Wilson, S.A. Thibeault, J.E. Nealy, M.Y. Kim, and R.L. Kiefer, Studies in Space Radiation Shield Performance. Proceedings of the Engineering & Architecture Symposium, Prairie View A&M Univ., 169-176 (1993).
- J.W. Wilson, M.R. Shavers, F.F. Badavi, J. Miller, J.L. Shinn, and R.C. Costen, Non-perturbative Methods In HZE Propagation. *Radiat. Res.* **140**, 241-248 (1994).
- J.W. Wilson, *et al.*, NUCFRG2: An Evaluation of the Semi-empirical Nuclear Fragmentation Database. NASA TP-3533 (1995b).
- N.E. Yanasak, W.R. Binns, A.C. Cummings, E.R. Christian, J.S. George, P.L. Hink, J. Klarmann , R.A. Leske, M. Lijowski, R.A. Mewaldt, E.C. Stone, T.T. von Rosenvinge, and M.E. Wiedenbeck, Implications for Cosmic Ray Propagation from ACE Measurements of Radioactive Clock Isotope Abundances, Proceedings of the 26th International Cosmic Ray Conference, Vol. 3, 9 (1999).
- C. Zeitlin, L. Heilbronn, J. Miller, S.E. Rademacher, T. Borak, T.R. Carter, K.A. Frankel, W. Schimmerling, and C.E. Stronach, Heavy Fragment Production Cross-sections from 1.05 GeV/nucleon ^{56}Fe in C, Al, Cu, Pb, and CH_2 Target. *Phys. Rev.* **C56**, 388-397 (1997).
- C. Zeitlin, A. Fukumura, L. Heilbronn, Y. Iwata, J. Miller, T. Murakami, Fragmentation Cross-sections of 600 MeV/nucleon ^{20}Ne on Elemental Targets. *Phys. Rev.* **C64**, 24902 (2001).
- C. Zeitlin, L. Heilbronn, J. Miller, A. Fukumura, Y. Iwata, and T. Murakami, Charge-changing and fragment production cross-sections of ^{28}Si on elemental targets from 400 MeV/nucleon to 1200 MeV/nucleon, LBNL-47655 (2002).
- C. Zeitlin, *et al.*, Results from MARIE (2003).

Table 1a: Comparison of HZETRN to Flight Measurements of GCR on NASA Space Shuttle and Russian Mir Space Station

Mission	DATE	Inclination	Altitude	Shielding	Dose, mGy/d			Dose Eq., mSv/d		
					Measured	Theory	%Difference	Measured	Theory	%Difference
STS-40	1991	39	293	Dloc2	0.052	0.048	7.7	0.13	0.16	-23.1
STS-49	1992	28.5	358	Dloc2	0.05	0.048	4.0	0.127	0.155	-22.0
STS-51	1993	28.5	296	Payload Bay	0.044	0.048	-9.1	0.144	0.154	-6.9
STS-57	1993	57	298	Payload Bay	0.113	0.109	3.5	0.422	0.434	-2.8
STS-57	1993	57	298	DLOC-2	0.138	0.11	20.3	0.414	0.37	10.6
Mir-18	1995	51.6	390	P	0.142	0.141	0.7	0.461	0.526	-14.1
STS-81	1997	51.6	400	0-sphere	0.147	0.135	8.2	0.479	0.521	-8.8
STS-81	1997	51.6	400	Poly 3-in	0.138	0.138	0.0	0.441	0.400	9.3
STS-81	1997	51.6	400	Poly 5-in	0.129	0.118	8.5	0.316	0.368	-16.5
STS-81	1997	51.6	400	Poly 8-in	0.128	0.113	11.7	0.371	0.323	12.9
STS-81	1997	51.6	400	Poly 12-in	0.116	0.111	4.3	0.290	0.298	-2.8
STS-89	1998	51.6	393	0-sphere	0.176	0.148	15.8	0.561	0.614	-9.4
STS-89	1998	51.6	393	Al 3-in	0.167	0.159	4.8	0.445	0.488	-9.7
STS-89	1998	51.6	393	Al 7-in	0.149	0.161	-8.1	0.529	0.617	-16.6
STS-89	1998	51.6	393	Al 9-in	0.171	0.162	5.3	0.492	0.541	-10.0

Table 1b: Comparisons of HZETRN Code to NASA Space Shuttle Phantom Torso Experiment on STS-91 (51.6 degree inclination by 390 km altitude). Measurements are taken from Badhwar *et al.* (2002).

<i>Organ</i>	<i>Measured (mGy)</i>	<i>Theory (mGy)</i>	<i>Theory* (mGy)</i>	<i>% Difference</i>	<i>% Difference*</i>
Brain	2.23	2.42	2.26	-8.5	-1.4
Bone Surface	2.16	2.36	2.21	-9.3	-2.1
Esophagus	1.71	1.79	1.67	-4.7	2.2
Lung	1.92	1.81	1.69	5.7	11.9
Stomach	2.05	2.08	1.94	-1.5	5.2
Liver	1.88	2.15	2.01	-14.4	-6.9
Spinal Column	1.65	1.98	1.85	-20.0	-12.1
Bone Marrow	1.75	1.98	1.85	-13.1	-5.7
Colon	1.71	1.9	1.78	-11.1	-3.8
Bladder	1.58	1.87	1.75	-18.4	-10.6
Gonad	1.75	1.85	1.73	-5.7	1.2
Skin/Breast	2.46	2.58	2.41	-4.9	2.0
Skin/Abdomen	2.35	2.58	2.41	-9.8	-2.6

*Comparisons that include TLD correction for LET response to heavy ions and neutrons.

Table 2a: Isotopic Composition of GCR Elements Z=3 to 12

<i>Isotope</i>	<i>Near-Earth Fraction</i>	<i>Source Fraction</i>
<i>Z=3</i>		
⁶ Li*	0.5	0.5
⁷ Li	0.5	0.5
<i>Z=4</i>		
⁷ Be*	0.5	0.5
⁹ Be	0.35	0.35
¹⁰ Be	0.15	0.15
<i>Z=5</i>		
¹⁰ B	0.31	0.2
¹¹ B	0.69	0.8
<i>Z=6</i>		
¹² C	0.92	0.999
¹³ C	0.08	0.001
<i>Z=7</i>		
¹⁴ N	0.48	0.78
¹⁵ N	0.57	0.22
<i>Z=8</i>		
¹⁶ O	0.946	0.985
¹⁷ O	0.027	0.008
¹⁸ O	0.027	0.007
<i>Z=10</i>		
²⁰ Ne	0.55	0.68
²¹ Ne	0.10	0.0
²² Ne	0.35	0.32
<i>Z=12</i>		
²⁴ Mg	0.64	0.74
²⁵ Mg	0.18	0.14
²⁶ Mg	0.18	0.13

*Data on solar modulation was insufficient and thus near-Earth and source composition are set equal.

Table 2b: Isotopic Composition of GCR Elements Z=13 to 20

<i>Isotope</i>	<i>Near-Earth Fraction</i>	<i>Source Fraction</i>
<i>Z=13</i>		
²⁶ Al	0.02	0.0
²⁷ Al	0.98	1.0
<i>Z=14</i>		
²⁸ Si	0.84	0.902
²⁹ Si	0.08	0.054
³⁰ Si	0.08	0.044
<i>Z=16</i>		
³² S	0.69	0.96
³³ S	0.15	0.02
³⁴ S	0.16	0.02
<i>Z=17</i>		
³⁵ Cl	0.52	1.0
³⁶ Cl	0.41	0.0
³⁷ Cl	0.26	0.0
<i>Z=18</i>		
³⁶ Ar	0.64	1.0
³⁷ Ar	0.03	0.0
³⁸ Ar	0.30	0.0
⁴⁰ Ar	0.03	0.0
<i>Z=20</i>		
⁴⁰ Ca	0.4	1.0
⁴¹ Ca	0.2	0.0
⁴² Ca	0.2	0.0
⁴³ Ca	0.2	0.0
⁴⁴ Ca	0.2	0.0

Table 2c: Isotopic Composition of GCR Elements Z=22 to 26

<i>Isotope</i>	<i>Near-Earth Fraction</i>	<i>Source Fraction</i>
<i>Z=22</i>		
⁴⁶ Ti*	0.27	0.27
⁴⁷ Ti	0.31	0.31
⁴⁸ Ti	0.30	0.30
⁴⁹ Ti	0.09	0.09
⁵⁰ Ti	0.03	0.03
<i>Z=23</i>		
⁴⁹ V*	0.53	0.53
⁵⁰ V	0.24	0.24
⁵¹ V	0.23	0.23
<i>Z=24</i>		
⁵⁰ Cr*	0.26	0.26
⁵¹ Cr	0.26	0.26
⁵² Cr	0.48	0.48
<i>Z=25</i>		
⁵³ Mn*	0.43	0.43
⁵⁴ Mn	0.17	0.17
⁵⁵ Mn	0.40	0.40
<i>Z=26</i>		
⁵⁴ Fe	0.076	0.055
⁵⁵ Fe	0.084	0.078
⁵⁶ Fe	0.763	0.792
⁵⁷ Fe	0.076	0.075

*Data on solar modulation was insufficient and thus near-Earth and source composition are set equal.

Table 3a: Isotope Grid Used in Present HZETRN Calculations for Elements Z=0-8

Index, j	Nuclei	Z	N	Mass Excess, MeV	Tz	Lifetime	Decay Mode
1	¹ n	0	1	8.071323	-1/2	614.6 s	β-
2	¹ H	1	0	7.28969	+1/2	Stable	
3	² H	1	1	13.13572	0	Stable	
4	³ H	1	2	14.949794	-1/2	12.33 y	β-
5	³ He	2	1	14.931203	+1/2	Stable	
6	⁴ He	2	2	2.424911	0	Stable	
7	⁶ He	2	4	17.5941	-1	0.807 s	β-
8	⁶ Li	3	3	14.0863	0	Stable	
9	⁷ Li	3	4	14.9077	-1/2	Stable	
11	⁸ Li	3	5	20.9452	-1	0.838 s	β-
13	⁹ Li	3	6	24.9540	-3/2	0.178 s	β-
10	⁷ Be	4	3	15.7695	+1/2	53.12 d	e
14	⁹ Be	4	5	11.3477	-1/2	Stable	
16	¹⁰ Be	4	6	12.6067	-1	1.51x10 ⁶ y	β-
19	¹¹ Be	4	7	20.174	-3/2	13.81 s	β-
12	⁸ B	5	3	22.92010	+1	0.770 s	β+
15	⁹ B	5	4	12.4158	+1/2	0.54 keV	2ap
17	¹⁰ B	5	5	12.0508	0	Stable	
20	¹¹ B	5	6	8.6680	-1/2	Stable	
22	¹² B	5	7	13.3689	-1	0.0202 s	β-
25	¹³ B	5	8	16.5623	-3/2	0.01736 s	β-
18	¹⁰ C	6	4	15.6986	+1	19.255 s	e+, β+
21	¹¹ C	6	5	10.6502	+1/2	0.0204 s	e+, β+
23	¹² C	6	6	0.0	0	Stable	
26	¹³ C	6	7	3.125011	-1/2	Stable	
28	¹⁴ C	6	8	3.019894	-1	5730 y	β-
31	¹⁵ C	6	9	9.8731	-3/2	2.449 s	β-
24	¹² N	7	5	17.3381	+1	0.0111 s	e+, β+
27	¹³ N	7	6	5.34546	+1/2	9.965 m	e+, β+
29	¹⁴ N	7	7	2.863419	0	Stable	
32	¹⁵ N	7	8	0.101508	-1/2	Stable	
34	¹⁶ N	7	9	5.6820	-1	7.13 s	β-
36	¹⁷ N	7	10	7.781	-3/2	4.173 s	β-
30	¹⁴ O	8	6	8.00646	+1	70.606 s	e+, β+
33	¹⁵ O	8	7	2.8555	+1/2	122.24 s	e+, β+
35	¹⁶ O	8	8	-4.736998	0	Stable	
37	¹⁷ O	8	9	-0.80900	-1/2	Stable	
39	¹⁸ O	8	10	-0.7821	-1	Stable	
42	¹⁹ O	8	11	3.3322	-3/2	26.91 s	β-
45	²⁰ O	8	12	3.7969	-2	13.51 s	β-

Table 3b: Isotope Grid Used in Present HZETRN Calculations for Elements Z=9-14

Index, j	Nuclei	Z	N	Mass Excess, MeV	Tz	Lifetime	Decay Mode
38	¹⁷ F	9	8	1.95170	+1/2	64.49 s	e+, β+
40	¹⁸ F	9	9	0.8734	0	0.1098 s	e+, β+
43	¹⁹ F	9	10	-1.48740	-1/2	stable	
46	²⁰ F	9	11	-0.01740	-1	11.0 s	β-
48	²¹ F	9	12	-0.0476	-3/2	4.158 s	β-
41	¹⁸ Ne	10	8	5.319	+1	1.672 s	e+, β+
44	¹⁹ Ne	10	9	1.7510	+1/2	17.22 s	e+, β+
47	²⁰ Ne	10	10	-7.041929	0	stable	
49	²¹ Ne	10	11	-5.73172	-1/2	stable	
51	²² Ne	10	12	-8.02435	-1	stable	
53	²³ Ne	10	13	-5.15365	-3/2	37.24 s	β-
56	²⁴ Ne	10	14	-5.948	-2	3.38 m	β-
50	²¹ Na	11	10	-2.1843	+1/2	22.49 s	e+, β+
52	²² Na	11	11	-5.1822	0	2.6019 y	e+, β+
54	²³ Na	11	12	-9.52950	-1/2	stable	
57	²⁴ Na	11	13	-8.41762	-1	14.959 h	β-
59	²⁵ Na	11	14	-9.3575	-3/2	59.1 s	β-
62	²⁶ Na	11	15	-6.902	-2	1.072 s	β-
55	²³ Mg	12	11	-5.4727	+1/2	11.317 s	e+, β+
58	²⁴ Mg	12	12	-13.93340	0	stable	
60	²⁵ Mg	12	13	-13.19275	-1/2	stable	
63	²⁶ Mg	12	14	-16.21451	-1	stable	
66	²⁷ Mg	12	15	-14.58654	-3/2	9.458 m	β-
69	²⁸ Mg	12	16	-15.0188	-2	20.91 h	β-
61	²⁵ Al	13	12	-8.9158	+1/2	7.183 s	e+, β+
64	²⁶ Al	13	13	-12.21032	0	7.17x10 ⁵ y	e+, β+
67	²⁷ Al	13	14	-17.19686	-1/2	stable	
70	²⁸ Al	13	15	-16.85058	-1	2.241 m	β-
72	²⁹ Al	13	16	-18.2155	-3/2	6.56 m	β-
75	³⁰ Al	13	17	-15.872	-2	3.60 s	β-
65	²⁶ Si	14	12	-7.145	+1	2.234 s	e+, β+
68	²⁷ Si	14	13	-12.38503	+1/2	4.16 s	e+, β+
71	²⁸ Si	14	14	-21.49283	0	stable	
73	²⁹ Si	14	15	-21.89506	-1/2	stable	
76	³⁰ Si	14	16	-24.43292	-1	stable	
79	³¹ Si	14	17	-22.94899	-3/2	0.1573 s	β-
82	³² Si	14	18	-24.0809	-2	150 y	β-
85	³³ Si	14	19	-20.492	-5/2	6.18 s	β-

Table 3c: Isotope Grid Used in Present HZETRN Calculations for Elements Z=15-19

Index, j	Nuclei	Z	N	Mass Excess, MeV	Tz	Lifetime	Decay Mode
74	²⁹ P	15	14	-16.9519	+1/2	4.140 s	e+, β+
77	³⁰ P	15	15	-20.2006	0	2.498 m	e+, β+
80	³¹ P	15	16	-24.44101	-1/2	stable	
83	³² P	15	17	-24.30534	-1	14.262 d	β-
86	³³ P	15	18	-26.3377	-3/2	25.34 d	β-
89	³⁴ P	15	19	-24.558	-2	12.43 s	β-
92	³⁵ P	15	20	-24.8576	-5/2	47.3 s	β-
78	³⁰ S	16	14	-14.063	+1	1.178 s	e+, β+
81	³¹ S	16	15	-19.0449	+1/2	2.572 s	e+, β+
84	³² S	16	16	-26.01594	0	Stable	
87	³³ S	16	17	-26.58620	-1/2	Stable	
90	³⁴ S	16	18	-29.93181	-1	Stable	
93	³⁵ S	16	19	-28.84633	-3/2	87.32 d	β-
96	³⁶ S	16	20	-30.66396	-2	Stable	
99	³⁷ S	16	21	-26.89622	-5/2	5.05 m	β-
103	³⁸ S	16	22	-26.861	-2	170.3 m	β-
88	³³ Cl	17	16	-21.0035	+1/2	2.511 s	e+, β+
91	³⁴ Cl	17	17	-24.443961	0	1.5264 s	e+, β+
94	³⁵ Cl	17	18	-29.01351	-1/2	Stable	
97	³⁶ Cl	17	19	-29.52189	-1	3.01x10 ⁵ y	β-
100	³⁷ Cl	17	20	-31.76152	-3/2	Stable	
104	³⁸ Cl	17	21	-29.79798	-2	37.34 m	β-
108	³⁹ Cl	17	22	-29.7998	-5/2	55.60 m	β-
95	³⁵ Ar	18	17	-23.0482	+1/2	1.775 s	e+, β+
98	³⁶ Ar	18	18	-30.23046	0	Stable	
101	³⁷ Ar	18	19	-30.9480	-1/2	35.04 d	e
105	³⁸ Ar	18	20	-34.7148	-1	Stable	
109	³⁹ Ar	18	21	-33.242	-3/2	269 y	β-
112	⁴⁰ Ar	18	22	-35.039889	-2	Stable	
115	⁴¹ Ar	18	23	-33.0673	-5/2	109.34 m	β-
118	⁴² Ar	18	24	-34.420	-3	32.9 y	β-
102	³⁷ K	19	18	-24.79926	+1/2	1.226 s	e+, β+
106	³⁸ K	19	19	-28.8017	0	7.636 m	e+, β+
110	³⁹ K	19	20	-33.80684	-1/2	Stable	
113	⁴⁰ K	19	21	-33.53502	-1	1.277x10 ⁹ y	β-
116	⁴¹ K	19	22	-35.55887	-3/2	Stable	
119	⁴² K	19	23	-35.0213	-2	12.36 h	β-
122	⁴³ K	19	24	-36.593	-5/2	22.3 h	β-

Table 3d: Isotope Grid Used in Present HZETRN Calculations for Elements Z=20-23

Index, j	Nuclei	Z	N	Mass Excess, MeV	Tz	Lifetime	Decay Mode
107	³⁸ Ca	20	18	-22.059	+1	0.440 s	e+, β+
111	³⁹ Ca	20	19	-27.2763	+1/2	0.8596 s	e+, β+
114	⁴⁰ Ca	20	20	-34.84611	0	Stable	
117	⁴¹ Ca	20	21	-35.1375	-1/2	1.03x10 ⁵ y	e
120	⁴² Ca	20	22	-38.5468	-1	Stable	
123	⁴³ Ca	20	23	-38.4084	-3/2	Stable	
125	⁴⁴ Ca	20	24	-41.4691	-2	Stable	
128	⁴⁵ Ca	20	25	-40.8125	-5/2	162.61 d	β-
131	⁴⁶ Ca	20	26	-43.1350	-3	Stable	
121	⁴² Sc	21	21	-32.12109	0	0.681 s	e+, β+
124	⁴³ Sc	21	22	-36.1876	-1/2	3.891 h	e+, β+
126	⁴⁴ Sc	21	23	-37.8158	-1	3.927 h	e+,β+
129	⁴⁵ Sc	21	24	-41.0694	-3/2	stable	
132	⁴⁶ Sc	21	25	-41.7587	-2	83.79 d	β-
135	⁴⁷ Sc	21	26	-44.3317	-5/2	3.3492 d	β-
138	⁴⁸ Sc	21	27	-44.493	-3	43.67 h	β-
127	⁴⁴ Ti	22	22	-37.5483	0	63 y	e
130	⁴⁵ Ti	22	23	-39.0069	-1/2	184.8 m	e+, β+
133	⁴⁶ Ti	22	24	-44.1254	-1	Stable	
136	⁴⁷ Ti	22	25	-44.9318	-3/2	Stable	
139	⁴⁸ Ti	22	26	-48.4871	-2	Stable	
142	⁴⁹ Ti	22	27	-48.5581	-5/2	Stable	
145	⁵⁰ Ti	22	28	-51.4259	-3	stable	
134	⁴⁶ V	23	23	-37.074	0	0.422 s	e+, β+
137	⁴⁷ V	23	24	-42.0040	-1/2	32.6 m	e+, β+
140	⁴⁸ V	23	25	-44.4747	-1	15.9735 d	e+, β+
143	⁴⁹ V	23	26	-47.9562	-3/2	330 d	e
146	⁵⁰ V	23	27	-49.2177	-2	1.4x10 ¹⁷ y	e+, β+
149	⁵¹ V	23	28	-52.1976	-5/2	Stable	
152	⁵² V	23	29	-51.4375	-3	3.743 m	β-

Table 3e: Isotope Grid Used in Present HZETRN Calculations for Elements Z=24-28

Index, j	Nuclei	Z	N	Mass Excess, MeV	Tz	Lifetime	Decay Mode
141	⁴⁸ Cr	24	24	-42.815	0	21.56 h	e+, β+
144	⁴⁹ Cr	24	25	-45.3256	-1/2	42.3 m	e+, β+
147	⁵⁰ Cr	24	26	-50.2546	-1	>1.8x10 ¹⁷ y	e
150	⁵¹ Cr	24	27	-51.4449	-3/2	27.7025 d	e
153	⁵² Cr	24	28	-55.4131	-2	Stable	
155	⁵³ Cr	24	29	-55.2810	-5/2	Stable	
158	⁵⁴ Cr	24	30	-56.9287	-3	Stable	
148	⁵⁰ Mn	25	25	-42.6216	0	0.284 s	e+, β+
151	⁵¹ Mn	25	26	-48.2371	-1/2	0.0462 s	e+, β+
154	⁵² Mn	25	27	-50.7013	-1	5.591 d	e+, β+
156	⁵³ Mn	25	28	-54.6840	-3/2	3.74x10 ⁶	e
159	⁵⁴ Mn	25	29	-55.5516	-2	312.3 d	e+, β+
161	⁵⁵ Mn	25	30	-57.7067	-5/2	Stable	
157	⁵³ Fe	26	27	-50.9414	-1/2	0.00851 s	e+, β+
160	⁵⁴ Fe	26	28	-56.2485	-1	Stable	
162	⁵⁵ Fe	26	29	-57.4751	-3/2	2.73 y	e
164	⁵⁶ Fe	26	30	-60.6013	-2	Stable	
167	⁵⁷ Fe	26	31	-60.1760	-5/2	Stable	
163	⁵⁵ Co	27	28	-54.0239	-1/2	17.53 h	e+,β+
165	⁵⁶ Co	27	29	-56.0353	-1	77.27 d	e+, β+
168	⁵⁷ Co	27	30	-59.3400	-3/2	271.79 d	e
166	⁵⁶ Ni	28	28	-53.900	0	6.077 d	e+, β+
169	⁵⁷ Ni	28	29	-56.0757	-1/2	35.60 h	e+, β+
170	⁵⁸ Ni	28	30	-60.2233	-1	Stable	

Table 4a: Elemental (Z) and Neutron Excess (Y) Dependence on GCR Dose Equivalent (cSV/yr) Behind 0 g/cm² of Aluminum Shielding

GCR Dose Equivalent per Year near Solar Minimum							
Z	Y<0	Y=0	Y=1	Y=2	Y=3	Y>3	Total-Z
0	0.00	0.00	0.00	0.00	0.00	0.00	0.00
1	9.15	0.21	0.00	0.00	0.00	0.00	9.37
2	0.50	3.61	0.00	0.00	0.00	0.00	4.11
3	0.00	0.04	0.04	0.00	0.00	0.00	0.08
4	0.05	0.00	0.03	0.01	0.00	0.00	0.10
5	0.00	0.23	0.36	0.00	0.00	0.00	0.60
6	0.00	3.72	0.31	0.00	0.00	0.00	4.03
7	0.00	0.74	0.99	0.00	0.00	0.00	1.73
8	0.00	11.26	0.32	0.32	0.00	0.00	11.90
9	0.00	0.00	0.38	0.00	0.00	0.00	0.38
10	0.00	2.33	0.45	1.48	0.00	0.00	4.26
11	0.00	0.00	1.33	0.00	0.00	0.00	1.33
12	0.00	6.89	1.86	1.88	0.00	0.00	10.63
13	0.00	0.12	2.34	0.00	0.00	0.00	2.46
14	0.00	11.22	1.08	1.06	0.00	0.00	13.36
15	0.00	0.00	0.85	0.00	0.00	0.00	0.85
16	0.00	2.87	0.59	0.65	0.00	0.00	4.11
17	0.00	0.00	0.52	0.41	0.26	0.00	1.19
18	0.00	1.37	0.06	0.68	0.00	0.05	2.15
19	0.00	0.00	1.71	0.00	0.00	0.00	1.71
20	0.00	1.57	0.00	0.78	0.78	0.78	3.92
21	0.00	0.00	0.00	0.00	1.00	0.00	1.00
22	0.00	0.00	0.00	1.02	1.17	1.59	3.78
23	0.00	0.00	0.00	0.00	1.00	0.89	1.88
24	0.00	0.00	0.00	1.02	1.02	1.89	3.93
25	0.00	0.00	0.00	0.00	1.26	1.67	2.92
26	0.00	0.00	0.00	2.05	2.26	22.50	26.80
27	0.00	0.00	0.00	0.00	0.10	0.00	0.10
28	0.00	0.00	0.00	1.45	0.00	0.00	1.45
Total-Y	9.70	46.18	13.22	12.81	8.85	29.35	120.11

Table 4b: Elemental (Z) and Neutron Excess (Y) Dependence on GCR Dose Equivalent (cSv/yr) Behind 5 g/cm² of Aluminum Shielding

GCR Dose Equivalent per Year near Solar Minimum							
Z	Y<0	Y=0	Y=1	Y=2	Y=3	Y>3	Total-Z
0	0.00	0.00	0.00	0.65	0.00	0.00	0.65
1	15.03	2.56	1.74	0.00	0.00	0.00	19.33
2	2.48	15.60	0.00	0.00	0.00	0.00	18.08
3	0.00	0.04	0.04	0.00	0.00	0.00	0.09
4	0.05	0.00	0.04	0.02	0.00	0.00	0.12
5	0.00	0.23	0.34	0.00	0.00	0.00	0.58
6	0.03	3.14	0.29	0.01	0.00	0.00	3.47
7	0.01	0.62	0.83	0.01	0.00	0.00	1.48
8	0.07	8.67	0.27	0.27	0.00	0.00	9.28
9	0.01	0.03	0.31	0.01	0.01	0.00	0.37
10	0.03	1.69	0.37	1.10	0.01	0.00	3.20
11	0.01	0.06	0.99	0.04	0.01	0.00	1.11
12	0.05	4.71	1.33	1.34	0.01	0.00	7.44
13	0.01	0.15	1.66	0.03	0.01	0.00	1.87
14	0.06	7.46	0.77	0.75	0.01	0.00	9.06
15	0.00	0.02	0.60	0.04	0.02	0.01	0.70
16	0.02	1.86	0.42	0.48	0.02	0.01	2.82
17	0.00	0.02	0.38	0.32	0.21	0.01	0.93
18	0.01	0.89	0.08	0.51	0.04	0.06	1.59
19	0.00	0.02	1.12	0.04	0.04	0.04	1.27
20	0.01	1.03	0.03	0.58	0.57	0.58	2.81
21	0.00	0.00	0.02	0.05	0.70	0.08	0.85
22	0.00	0.01	0.03	0.72	0.81	1.12	2.69
23	0.00	0.00	0.02	0.05	0.71	0.66	1.44
24	0.00	0.00	0.03	0.68	0.73	1.33	2.77
25	0.00	0.00	0.02	0.05	0.88	1.23	2.18
26	0.00	0.00	0.03	1.34	1.50	13.90	16.77
27	0.00	0.00	0.00	0.01	0.06	0.00	0.08
28	0.00	0.00	0.01	0.87	0.00	0.00	0.88
Total-Y	17.88	48.84	11.80	9.95	6.37	19.03	113.88

Table 4c: Elemental (Z) and Neutron Excess (Y) Dependence on GCR Dose Equivalent (cSv/yr) Behind 20 g/cm² of Aluminum Shielding

GCR Dose Equivalent per Year near Solar Minimum							
Z	Y<0	Y=0	Y=1	Y=2	Y=3	Y>3	Total-Z
0	0.00	0.00	0.00	2.00	0.00	0.00	2.00
1	18.95	3.09	2.21	0.00	0.00	0.00	24.24
2	2.67	17.03	0.00	0.00	0.00	0.00	19.69
3	0.00	0.03	0.03	0.00	0.00	0.00	0.07
4	0.04	0.00	0.04	0.02	0.00	0.00	0.10
5	0.00	0.13	0.21	0.00	0.00	0.00	0.35
6	0.05	1.51	0.13	0.02	0.00	0.00	1.72
7	0.02	0.41	0.38	0.01	0.00	0.00	0.83
8	0.11	3.69	0.12	0.11	0.00	0.00	4.02
9	0.01	0.04	0.17	0.02	0.01	0.00	0.26
10	0.04	0.75	0.16	0.46	0.01	0.00	1.43
11	0.01	0.09	0.45	0.05	0.02	0.00	0.62
12	0.08	1.84	0.52	0.50	0.01	0.00	2.95
13	0.02	0.12	0.69	0.04	0.02	0.00	0.89
14	0.08	2.57	0.29	0.26	0.02	0.01	3.22
15	0.01	0.04	0.26	0.05	0.03	0.01	0.39
16	0.03	0.71	0.15	0.18	0.03	0.02	1.12
17	0.00	0.02	0.19	0.12	0.08	0.02	0.44
18	0.01	0.34	0.07	0.19	0.05	0.04	0.70
19	0.00	0.03	0.39	0.06	0.05	0.05	0.58
20	0.02	0.47	0.05	0.20	0.19	0.19	1.11
21	0.00	0.01	0.03	0.07	0.29	0.10	0.49
22	0.00	0.01	0.04	0.30	0.33	0.46	1.14
23	0.00	0.00	0.03	0.06	0.30	0.31	0.71
24	0.00	0.01	0.04	0.26	0.31	0.55	1.16
25	0.00	0.00	0.02	0.06	0.36	0.55	1.00
26	0.00	0.00	0.03	0.43	0.53	4.13	5.13
27	0.00	0.00	0.00	0.01	0.02	0.00	0.04
28	0.00	0.00	0.01	0.24	0.00	0.00	0.25
Total-Y	22.15	32.94	6.69	5.73	2.68	6.45	76.64

Table 5: Annual Fluence of Several Unstable GCR Nuclei Versus Depth of Aluminum Shielding Near Solar Minimum ($\Phi=428$ MV)

Nuclei	<i>Fluence per cm² per year</i>			
	0, g/cm ²	2, g/cm ²	5, g/cm ²	20, g/cm ²
⁶ He	0.0	9.1x10 ¹	2.1x10 ²	5.6x10 ²
⁸ Li	0.0	1.0x10 ³	2.2x10 ³	5.4x10 ³
⁹ Li	0.0	3.0x10 ¹	7.2x10 ¹	1.8x10 ²
¹⁰ Be	8.8x10 ³	9.1x10 ³	9.3x10 ³	8.8x10 ³
¹⁴ C	0.0	7.1x10 ²	1.7x10 ³	3.4x10 ³
¹⁸ O	9.9x10 ³	9.3x10 ³	8.4x10 ³	5.1x10 ³
²⁶ Al	5.7x10 ²	7.6x10 ²	9.4x10 ²	1.0x10 ³
³⁶ Cl	8.1x10 ²	7.7x10 ²	7.1x10 ³	4.4x10 ²

REPORT DOCUMENTATION PAGE			Form Approved OMB No. 0704-0188	
Public reporting burden for this collection of information is estimated to average 1 hour per response, including the time for reviewing instructions, searching existing data sources, gathering and maintaining the data needed, and completing and reviewing the collection of information. Send comments regarding this burden estimate or any other aspect of this collection of information, including suggestions for reducing this burden, to Washington Headquarters Services, Directorate for Information Operations and Reports, 1215 Jefferson Davis Highway, Suite 1204, Arlington, VA 22202-4302, and to the Office of Management and Budget, Paperwork Reduction Project (0704-0188), Washington, DC 20503.				
1. AGENCY USE ONLY (Leave Blank)		2. REPORT DATE February 2003		3. REPORT TYPE AND DATES COVERED NASA Technical Paper
4. TITLE AND SUBTITLE PHYSICS OF THE ISOTOPIC DEPENDENCE OF GCR FLUENCE BEHIND SHIELDING			5. FUNDING NUMBERS	
6. AUTHOR(S) Francis A. Cucinotta*, John W. Wilson**, Premkumar Saganti*, Xiaodong Hu1, Myung-Hee Y. Kim*, Timothy Cleghorn*, Cary Zeitlin***, and Ram K. Tripathi**				
7. PERFORMING ORGANIZATION NAME(S) AND ADDRESS(ES) Lyndon B. Johnson Space Center Houston, Texas 77058			8. PERFORMING ORGANIZATION REPORT NUMBERS S-891	
9. SPONSORING/MONITORING AGENCY NAME(S) AND ADDRESS(ES) National Aeronautics and Space Administration Washington, DC 20546-0001			10. SPONSORING/MONITORING AGENCY REPORT NUMBER TP-2003-210792	
11. SUPPLEMENTARY NOTES *NASA, Johnson Space Center, Houston TX, 77058; **NASA, Langley Research Center, Hampton VA, 23664; ***3Lawrence Berkeley National Laboratory, Berkeley, CA 94720				
12a. DISTRIBUTION/AVAILABILITY STATEMENT Available from the NASA Center for AeroSpace Information (CASI) 7121 Standard Hanover, MD 21076-1320 subject category 93			12b. DISTRIBUTION CODE	
13. ABSTRACT (Maximum 200 words) For over 25 years NASA has supported the development of space radiation transport models for shielding applications. The NASA space radiation transport model now predicts dose and dose equivalent in Earth and Mars orbit to an accuracy of +20%. However, larger error may occur in particle fluence predictions and there is interest in further assessments and improvements in NASA's space radiation transport model. In this paper we consider the effects of the isotopic composition of the primary galactic cosmic rays (GCR) and the isotopic dependence of nuclear fragmentation cross-sections on the solution to transport models used for shielding studies. Satellite measurements are used to describe the isotopic composition of the GCR. Using NASA's quantum multiple-scattering theory of nuclear fragmentation (QMSFRG) and high-charge and energy (HZETRN) transport code, we study the effect of the isotopic dependence of the primary GCR composition and secondary nuclei on shielding calculations. The QMSFRG is shown to accurately describe the iso-spin dependence of nuclear fragmentation. The principle finding of this study is that large errors (+100%) will occur in the mass-fluence spectra when comparing transport models that use a complete isotopic-grid (~170 ions) to ones that use a reduced isotopic-grid, for example the 59 ion-grid used in the HZETRN code in the past, however less significant errors (<20%) occur in the elemental-fluence spectra. Because a complete isotopic-grid is readily handled on small computer workstations and is needed for several applications studying GCR propagation and scattering, it is recommended that they be used for future GCR studies.				
14. SUBJECT TERMS radiation, galactic cosmic rays, fluence, radiation absorption, radiation shielding, radiation transport			15. NUMBER OF PAGES 50	
16. PRICE CODE				
17. SECURITY CLASSIFICATION OF REPORT Unclassified		18. SECURITY CLASSIFICATION OF THIS PAGE Unclassified		19. SECURITY CLASSIFICATION OF ABSTRACT Unclassified
20. LIMITATION OF ABSTRACT Unlimited				
